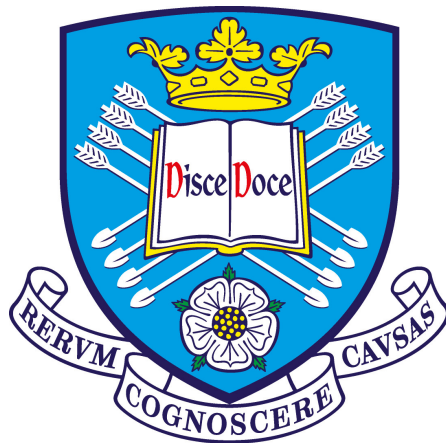# How fast do white dwarfs accrete their companions?

James F. Wild

Department of Physics & Astronomy
The University of Sheffield

*A dissertation submitted in candidature for the degree of
Doctor of Philosophy at the University of Sheffield*

Submission month year

"

Sometimes a problem that initially looks hopelessly complicated turns out to have a surprisingly simple solution (though the reverse is probably more common).

"

— Nick Bostrom

# My Shitlist

# Contents

# List of Figures

# List of Tables

# Declaration

I declare that, unless otherwise stated, the work presented in this thesis is my own. No part of this thesis has been accepted or is currently being submitted for any other qualification at the University of Sheffield or elsewhere.

Much of the work presented here has already been published and can be found in [YOUR PAPERS]

# Acknowledgments

Let this be a surprise...

# Summary

300 words max

Possibly, at the end of this section, put a little table of the acronyms I use?

# Chapter 1

# Background, context, and motivation

Cataclysmic Variable (CV) systems consist of a white dwarf primary, and a lower mass red dwarf secondary star. The two are in extremely close proximity, such that the outer layers of the secondary are gradually accreted onto the white dwarf; this mass transfer process affects the evolution of both stars, in particular the donor, and is the main driving mechanism for the evolution of the system as a whole. The accretion also gives two further key features of a CV: an accretion disc around the white dwarf, and a shock-heated bright spot region where accreted donor material impacts the outer rim of the disc. Systems actively undergoing mass transfer are important to our understanding of stellar evolution, as a diversity of stars will experience a mass transfer phase, and losing mass strongly influences a stars' evolutionary path and must be accounted for. Of such systems, CVs in particular are interesting as modelling their eclipse lightcurves can yield precise, independent measures of both stars' mass and radius (Wood & Crawford, 1986; Littlefair et al., 2008; Savoury et al., 2011). Further, since the donor stars' evolution is completely dominated by its mass loss, CVs provide a window into binary evolution (Knigge, 2006).

Since CVs involve poorly understood physics, such as magnetism and the structure and evolution of low mass stars, but are also open to comprehensive analysis, they provide an excellent test-bed for binary evolution modelling, and the difficult processes that contribute to them. Unfortunately, whilst modelling most of a CV's life is now possible (Paxton et al., 2015), the field has yet to produce physically motivated models capable of accurately reproducing either the CV population distribution, or complete evolutionary track, indicating some shortfalls in our understanding. Of most significance to this work is the problem of missing Angular Momentum Loss (AML), where CVs with extremely low mass donor stars appear to be losing angular momentum much faster than our models predict. This first chapter will summarise the current understanding of CV formation and evolution, and the current state of CV modelling.

The bulk of this thesis is focused on two elements: firstly, the sample of well-characterised (i.e. measured masses and radii for both stars, white dwarf temperature and surface gravity, orbital period, and inclination) eclipse modelled CVs is small - only 18 systems prior to this work. I characterise an additional XXX systems. While this is still a small sample, it is now enough for approximate statistical analysis. Second, using stellar models, I affirm the observations that the canonical CV evolutionary track fails at periods shorter than $\sim 2.5$ hours,

> Do I really need a reference for this? Probably just reference that "on cataclysmic variables" or whatever that book was. You know the one.

> Put in your CV schematic here. Maybe update it and try to make it prettier?

> ref here - was it a savoury paper? Perhaps pala? I cant remember

> ref

> Put in here how many systems

> cite this

and produce an empirical correction to predicted AML, as a function of donor mass. Through this, I hope to constrain the possible sources of missing AML.

## 1.1 Roche geometry

Before discussing the formation, structure, and evolution of CVs, it is critical to understand Roche lobes. In a two-body orbital system, the Roche potential of a point is an effective potential in the non-inertial, co-rotating frame of reference. It is given by the sum of the gravitational potential energies due to the two masses, and the potential energy arising from centrifugal force. This can be described mathematically for each position vector:

$$\phi = -\frac{GM_1}{|\mathbf{r} - \mathbf{r}_1|} - \frac{GM_2}{|\mathbf{r} - \mathbf{r}_2|} - \frac{1}{2}(\mathbf{\Omega} \times \mathbf{r})^2 \tag{1.1}$$

Where $\phi$ is the Roche potential, G is the gravitational constant, $\mathbf{r}$ is the position vector being considered, and $\mathbf{\Omega}$ is the angular momentum vector of the binary. $M_{1,2}$ and $\mathbf{r}_{1,2}$ are the masses and position vectors of the two orbiting bodies.

Near to each of the bodies, the gravitational potential is large and negative, and dominates the Roche potential. This becomes *less negative* as we move away from that body. Conversely, angular momentum is less negative closer to the center of mass, and more negative as we move away from the system and larger velocities are required to co-rotate. Broadly, there are then three regimes: a very negative Roche potential near each of the two bodies, a less negative region immediately surrounding the two bodies, and a very negative region far from the two bodies. The overall potential is smooth, so joining the three regions requires a ridge encircling the orbiting bodies, and a saddle between them. Figure 1.1 shows this graphically. The saddle is centred on the first Lagrangian point, $L_1$, and is the point at which a small (co-rotating) mass is attracted equally and oppositely by both bodies. We can trace the line of constant potential that passes through the $L_1$ point, giving two teardrops joined at the tips. The teardrop that encapsulates a star is known as its Roche lobe. Matter that extends beyond the Roche lobe is no longer gravitationally bound to its parent body, and will either fall onto its companion via the $L_1$ point, or otherwise be ejected from the star. This material will no longer be in a stable orbit, so will either be ejected from the system, or find a new higher orbit where the two-body effects are negligible.

Proof read this section

Make your own version of this figure - this one is blurry and ugly
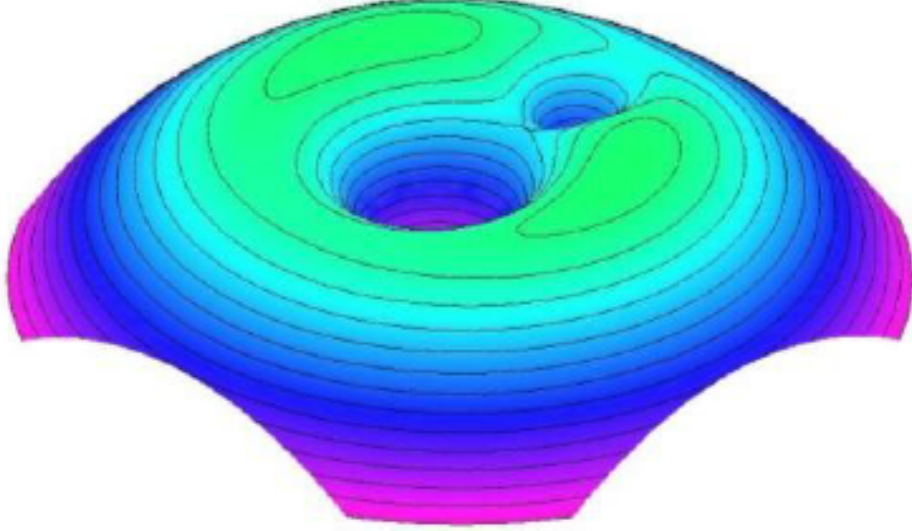
Figure 1.1: Showing the Roche potential in the neighbourhood of the binary system. Each line represents a line of equipotential. Taken from Cerutti et al. (2007)

The shape of the Roche lobes are non-trivial to calculate, and must be done numerically. However, approximations exist for the volume-equivalent radius of a Roche lobe (that is, the radius of a sphere of equivalent volume). Most commonly used is the Eggleton (1983) approximation,

$$\frac{R_L}{a} = \frac{0.49q^{2/3}}{0.6q^{2/3} + \ln(1 + q^{1/3})} \tag{1.2}$$

where $a$ is the orbital separation, and $q$ is the mass ratio of the system, $M_2/M_1$. In CVs, where the secondary star is completely filling its Roche lobe, $R_L$ makes for a good approximation for the secondary stars' radius.

## 1.2 CV formation

The formation of a CV begins with a binary system forming at a distance of $\sim 100R_\odot$. Crucially, the stars differ significantly in mass, one typically being $< 1M_\odot$ and the other $> 1M_\odot$ (Ritter, 2012). The lifespan of a star falls as its mass increases, so the larger star evolves faster than its companion, ascending the

red giant branch after a few Gyrs and expanding to fill its Roche lobe. As the outer layers contact the Roche lobe, stellar material crosses the boundary between being gravitationally bound to the donor and being ejected from its surface. Once the outer layers of the primary contact the Roche lobe, the $L_1$ point forms a locus for mass to move from the massive, evolved star onto the less evolved secondary star.

As mass moves away from the primary, and away from the centre of mass of the system, it gains angular momentum. However, because angular momentum is conserved within the binary this is offset by a drop in separation, $a$, and the radius of the Roche Lobe, $R_L$, contracts. *More* matter is now outside the primary Roche lobe, encouraging further mass transfer and hence further reduction in orbital separation (Ritter, 2010a).

With this positive feedback loop, the primary can rapidly transfer its whole envelope, though the transfer rate $\dot{M}$ is too high to for all of this to be properly assimilated into the primary surface. The process is very rapid – so rapid that models have been unable to properly resolve it, but is probably $\sim 10^2 - 10^3$ years in duration (Ritter, 2012). With this influx of mass, the secondary star grows and the accreted matter forms a thick, bloated, and deeply convective envelope on the star. The increased radius of the secondary brings the two bodies into contact (Ritter, 2010a) and the stars enter a common envelope phase of evolution. See Paczynski (1976) for an original reference on common envelope evolution, or Ivanova et al. (2020) for a recent review of the topic. For detail on this phase as it relates to CVs, see Taam et al. (1978); Webbink (1984); Zorotovic & Schreiber (2010); Passy et al. (2011).

The common envelope phase transfers much of the secondary stars' angular momentum to the shared envelope, though the mechanism for this is poorly understood (De Marco et al., 2011). If the common envelope is substantial enough, the reduction in separation between the two stellar cores can be completely reduced, and the two merge together. If it is not, the entire envelope is stripped from the stars, and the two are left in a compact orbit. CV systems are the product of the latter scenario - the common envelope is ejected via a strong wind, leaving the remnant core of the primary as a white dwarf, and a low mass secondary companion M dwarf.

The common envelope phase can be parameterised with the energies involved, namely the gravitational binding energy of the envelope, $U_{\mathrm{bind}}$, and the change

in the angular momentum contained in the orbit before and after the common envelope phase, $\Delta U_{\mathrm{orb}}$, as the common envelope efficiency parameter, $\alpha$.

$$\alpha = \frac{U_{\mathrm{bind}}}{\Delta U_{\mathrm{orb}}} \tag{1.3}$$

This is known as the $\alpha$ formalism (De Marco et al., 2011), and is a good illustration of how poorly we understand CE evolution. $\alpha$ should be a metric we can predict with models, but this has proven very challenging and several competing frameworks exist (Ivanova et al., 2020).

The energy needed to liberate the envelope is expected to come from the angular momentum of the binary, but some systems have been observed and characterised with $\alpha > 1$. This suggests that other sources, like the thermal output of the stars, contributes to the envelope ejection (De Marco et al., 2011; Ivanova et al., 2013). Common envelope evolution remains a very difficult problem to solve, and only approximate models currently exist (Ivanova et al., 2020), but the following scenario is generally accepted as likely in the case of CVs.

During the common envelope phase, the envelope is expelled into a planetary nebula (Ritter, 2012), and $\alpha$ in the case of a proto-CV hass been loosely estimated to be $\sim 0.2 - 0.6$ (Politano & Weiler, 2007), and some evidence exists for lower $q$ systems having larger $\alpha$ (Passy, 2013). The ejecta carries with it angular momentum, causing $a$ to quickly fall from $\sim 100 R_\odot$ to less than $1 R_\odot$, leaving behind a white dwarf and a low mass companion star – usually a cool, red M dwarf – in an extremely compact orbit, typically a few $R_\odot$. At this point, the red dwarf detaches from its Roche lobe and mass transfer is shut off. Angular momentum is shed through magnetic braking and gravitational wave braking until the donor comes into contact with its Roche lobe. Mass transfer can then resume, though this time in the more stable secondary-to-primary direction. The system is now a CV, and its evolution from here will be dominated by AML and mass transfer, detailed in §1.3.1.

## 1.3   CV evolution

Initially, mass from the more massive star transferred to the smaller one, but once the system emerges from the common envelope phase, AML causes the orbit to tighten until the less massive red dwarf secondary fills its Roche lobe. This now

means that mass transfer is moving matter closer to the system's centre of mass, imparting angular momentum to the secondary as it does so. This causes the donor to retreat, and increases $R_L$. Hence, mass transfer now acts to decrease further transfer (Ritter, 2010a), rather than exacerbate it.

To resume mass transfer some mechanism is necessary to shed angular momentum and bring the secondary back in contact with its Roche lobe. Canonically, two mechanisms are thought to drive this; gravitational wave braking, and magnetic braking. AML drives the two bodies closer together and triggers mass transfer, and mass loss from the donor drives it to retreat from the white dwarf primary. These two processes find equilibrium when the donor is just barely overflowing its Roche lobe, and the angular momentum gained by the donor from mass transfer is offset by the AML from the system. The mass transfer timescale of the donor is much shorter than its nuclear timescale, so mass loss dominates its evolution and gives rise to a single, unified CV evolutionary path.

There is a further complicating factor to consider; while the secondary is losing mass, it is not in thermodynamic equilibrium. The outer layers are being lost, which reduces the pressure on the core and so reduces the rate of fusion. Above masses of $\sim 0.1 M_\odot$, the thermal timescale is much longer than the mass loss timescale (this is demonstrated in §3.3), so the star is unable to cool and contract to its equilibrium radius. This leaves the star hotter than it would be under zero mass loss, and so its radius increases in response to the mass loss, and a higher mass loss rate results in larger inflation. When the donor first connects to its Roche lobe, this causes an initial spurt of mass loss and an increase in orbital period, but reconnection quickly reoccurs and remains stable.

### 1.3.1  Sources of angular momentum loss

When two bodies orbit each other in space, the periodic warping of space-time produces gravitational waves. These waves carry energy away from the system, robbing it of angular momentum and reducing the orbital radius (Paczyński, 1967). In CVs, the rate of momentum loss from gravitational waves is small, so long timescales (by human standards) are needed to significantly alter the orbital period, $P$. The rate of change of the period, $\dot{P}$, should be possible to probe with long-baseline observations (e.g. Qian et al. 2007; Shafter & Bautista 2021), but are prone to large errors and are difficult to gather data for. However, this has not prevented some systems having their $\dot{P}$ inferred indirectly and a few such

characterisations have been done. Notably, Pala et al. (2020) recently inferred the mass loss rates (which directly relates to $\dot{P}$) of 42 CVs from HST spectra, using the white dwarf temperature and mass as diagnostics. In the near future, CV gravitational waves are expected to be visible to the LISA mission, and direct measurements of $\dot{P}$ at scale will become feasible (Meliani et al., 2000; Kalomeni et al., 2016).

Population synthesis models do not match observations with gravitational braking alone, and magnetic braking is thought to make up the deficit (e.g. Kolb (1993); Kolb & de Kool (1993); Davis et al. (2008); Garraffo et al. (2018b)). Additionally, Townsley & Gänsicke (2009), Pala et al. (2021) infer the mass transfer rate (a diagnostic of $\dot{P}$) from the white dwarf surface temperature, and find results inconsistent with pure gravitational braking.

If one of the stars has a strong magnetic field (often assumed to be the secondary, though white dwarfs can have strong 'frozen-in' magnetic fields (Tout, 2011)), any wind emanating from the system, which is made up of charged particles, and likely originating from the secondary, will couple with the magnetic field to some degree and carry some angular momentum away from the binary with it. In the case of a CV, the wind originates from the secondary star, and the magnetic field is often assumed to be associated with the secondary also, though white dwarfs can have strong 'frozen-in' magnetic fields (Tout, 2011).

A detailed description of the modern understanding of magnetic braking is given in §1.4, after the following outline of CV evolution. Some elements of CV evolution are necessary to understand magnetism in CVs.

### 1.3.2 Period evolution and key population features

Through careful observation, The orbital period of a CV can be measured by tracking either their spectroscopic radial velocities (e.g. Gänsicke et al. 2009), or the timings of repeating features in their lightcurves (e.g. Littlefair et al. 2008). Once this has been done for a large enough sample, a histogram of the periods can be plotted. This plot, shown in fig. 1.2, is important to understanding how a CV will evolve over time. There are three immediately obvious features of the plot;

- a long period cutoff, as the number of systems taper off after $\sim 12$hrs

- a period gap at $\sim 2 - 3$hrs

Stu disagrees - update your understanding here.

Is this wise? I think it's a catch 22 - I need MB to explain CV evolution, but I need to have talked about the long-P, Pgap, and short P CVs to really get into the MB weeds...
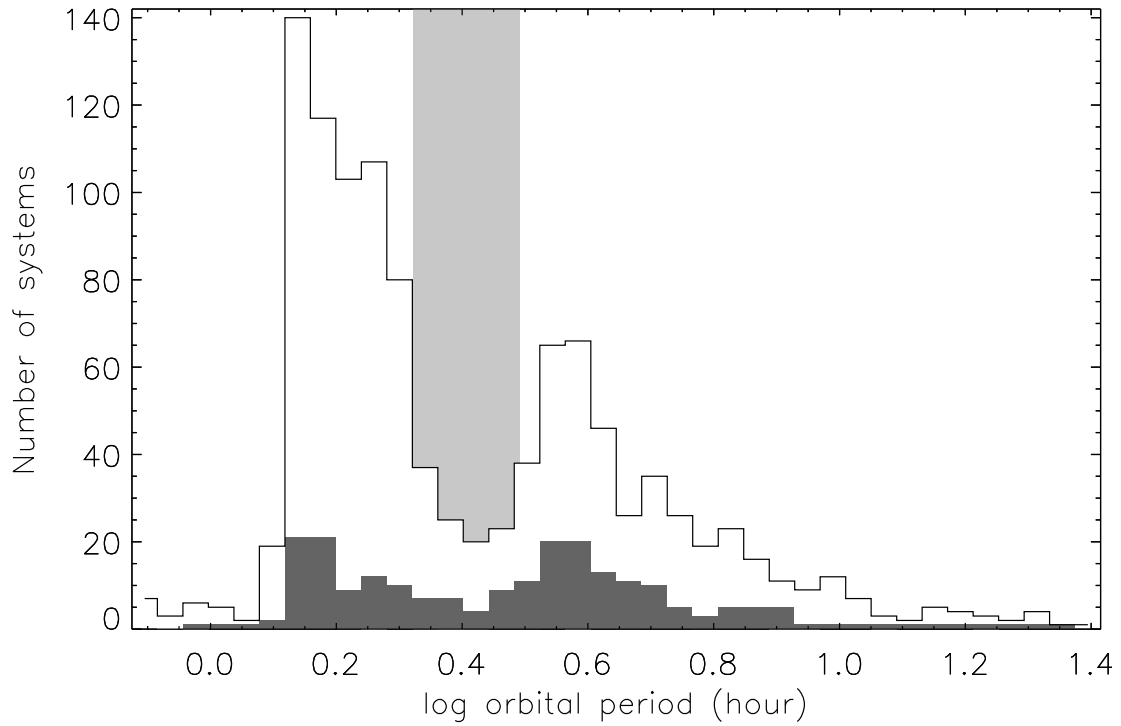
Figure 1.2: Reproduced from Southworth et al. (2015), Figure 14. The orbital period distribution of RKCat (Ritter, H. & Kolb, U., 2003) CVs identified by the SDSS (white histogram) and of the subset of these which are eclipsing (grey histogram). The light grey rectangle delineates the period gap at 2.1–3.1 hours. The periods have been collected into histogram bins which are of equal size in log space.

- a period minimum at $\sim 1$ hour, with a pile-up of systems just above it.

Each of these features are discussed in turn.

### 1.3.3 The period maximum

In order for a system be be a CV, mass must be transferring from a less massive star, onto a compact object, constraining the maximum value of $q$ to $\sim 1$, and demanding that the secondary extends out to $\sim R_L$.

There are two immediately obvious constraints for a CV. The mass ratio, $q = \frac{M_{\text{donor}}}{M_{\text{WD}}}$, must be less than 1 for stable mass transfer, and the donor radius must be approximately equal to the Roche radius. An additional constraint is that the maximum mass of a white dwarf is well known to be limited to $\leq 1.4 M_\odot$ before triggering thermonuclear runaway (Schönberg & Chandrasekhar, 1942).

An important feature of a Roche lobe is that for a fixed mass ratio, $q = \frac{M_1}{M_2}$, its radius, $R_L$, is roughly linearly dependant on the orbital separation, $a$. Recall the Eggleton approximation for a Roche lobe radius, Equation 1.2:

$$\frac{R_L}{a} = \frac{0.49 q^{2/3}}{0.6 q^{2/3} + \ln(1 + q^{1/3})} \tag{1.2}$$

Warner (1995) found that the average density, $\rho_{av}$, for objects that fill their $R_L$ follows a robust relationship;

$$\frac{\rho_{av}}{\rho_\odot} = 75.9 P_{orb}^{-2}(h) \tag{1.4}$$

Knigge et al. (2011) derived a connection between CV secondary mass and radius, $M_2$ & $R_L$. This can be manipulated to produce a mass-period relationship,

$$\rho_{av} = \frac{3 M_2}{4 \pi R_L^3} \simeq 75.9 P(h)^{-2} \tag{1.5}$$

$$\frac{R_L}{R_\odot} = C \cdot \left( \frac{M_2}{D \cdot M_\odot} \right)^\alpha \tag{1.6}$$

where $C$ and $D$ are constants for a particular regime, i.e., short-period, long-period, or period bouncer, and $\alpha$ is the mass-radius index (Knigge, 2011). Combining the above gives a pleasingly simple relationship.

$$M_2^{(1-3\alpha)} \propto P^{-2} \tag{1.7}$$

For long-period CVs, $\alpha = 0.67 \pm 0.04$ (Knigge et al., 2011), and equation 1.7 becomes $M_2^{1.01} \propto P^2$, and larger secondary masses require longer periods. The theoretical maximum secondary mass of $1.4 M_\odot$ corresponds to a period of $\sim 12$hrs, though in reality these higher masses are rarer and the frequency of CVs at these higher periods begins to drop much earlier, at $\sim 6$hrs (Gänsicke et al., 2009). Note while the above is specific to long-period systems, and $\alpha$ is a non-linear function of mass, and different values are needed for the period gap and short period regimes.

### 1.3.4 The period gap

Between periods of around 2-3 hours, there is a dramatic fall in the number of CVs we detect. Volume-limited samples indicate that this is a real effect and not a selection bias (Kolb et al., 1998). However, the origin of this gap in the period is something of an open problem.

Models indicate that long period systems ($P > 3$h) have far higher mass loss rates than short period systems ($P < 2$h) (Ritter, 1985). This suggests a significant change in braking mechanisms between the two regimes.

The disruption of magnetic braking was proposed early on to explain the period gap (Rappaport et al., 1983; Spruit & Ritter, 1983), and relatively shortly after Kolb & de Kool (1993) showed more quantitatively that a sub-class of purely gravitational braking CV systems does not reproduce the observed population. Historically, the standard evolutionary path of CVs has involved the secondary becoming fully convective which was thought to disrupt the magnetic field and so cease MB (Knigge et al., 2011), though this has frequently been questioned.

It is important to develop diagnostics for the nature of the period gap, and Smith & Dhillon (1998) show how spectral analysis could yield an accurate observed mass-radius relation for donor stars in CVs as evidence for MB, though they lacked the observations to apply their method. The mass-radius relation would later be carried out by Knigge et al. (2011). Davis et al. (2008) used population synthesis to demonstrate that, if the period gap is caused by disrupted MB, this may affect the mass function of quiescent CVs that are moving through the gap. They expect an excess of non-transferring CVs over low mass post-common envelope CVs that emerge from the common envelope phase directly into the period gap. These should form at a predictable rate across $q$, but due to the slow crossing of quiescent CVs, the latter 'pile up' in the gap - a detectable effect

observed by Zorotovic et al. (2011).

Disrupted MB has faced some difficulty in recent years. X-ray emission level is a diagnostic of magnetic flux (Pevtsov et al., 2003), and Wright & Drake (2016) found that the X-ray flux of CVs is similar between fully convective and non-convective main-sequence stars, implying a similar magnetic field strength. Furthermore, disagreement between observational and theoretical period gap and minimum locations (Knigge et al., 2011) has left the disrupted MB model an area of active research. Garraffo et al. (2018b) recently proposed that the magnetic field does not weaken, but rather becomes more complex which reduces the efficiency of MB. If this disruption does occur, the secondary can now contract on to its equilibrium radius, and quickly disconnects from its Roche lobe. The system then becomes quiescent, no longer presenting as a CV, but rather as an inert binary. As such, it is no longer included on the CV period diagram, and so the upper edge of the period gap develops.

The system is still subject to gravitational radiation, however, so gradually evolves back towards shorter periods. Once the secondary reconnects with its Roche lobe, mass transfer resumes and the system again presents itself as a CV, emerging from the period gap at a $\sim 2$hr period (Kolb, 2002).

### 1.3.5  The period minimum, and period bouncer systems

The period minimum was first predicted by Rappaport et al. (1982), and can be understood by considering the two governing timescales affecting the secondary. For donors with masses above $\sim 0.1 M_\odot$, the donor is contracting in response to mass loss. However, at a period of about 80 minutes (Ritter & Kolb, 1998; McAllister et al., 2019), $\tau_{\dot{M}}$ becomes longer than $\tau_{therm}$, causing the donor to lose mass adiabatically and expand rather than contract. This now allows the donor to remain in contact with its Roche Lobe when mass loss raises it to a higher orbit, and the system evolves to longer periods over time.

More quantitatively, as the components of a short period CV move closer together and the donor falls in mass, $\tau_{therm}$ and $\tau_{\dot{M}}$ become more out of balance, corresponding to $\alpha$ in equation 1.7 decreasing (Knigge, 2011). A main-sequence star will have $\alpha \sim 1$, but a secondary subjected to fast, adiabatic mass loss will have $\alpha \simeq -1/3$. Looking at the gradient of equation 1.7, the existence of a period

minimum can be easily seen.

$$\frac{\dot{P}}{P} = \frac{(3\alpha - 1)}{2} \frac{\dot{M_2}}{M_2} \tag{1.8}$$

When $\alpha \leq 1/3$, a negative $\dot{M}$ will produce a *positive* change in $P$, and the donor begins to retreat from the white dwarf (Rezzolla et al., 2001).

This has been confirmed by Knigge et al. (2011), who found that for period bouncer CVs, $\alpha = 0.21^{+0.05}_{-0.10}$, giving the following empirical version of equation 1.7 in the post-period minimum regime.

$$M_2 \propto P^{-5.4} \tag{1.9}$$

*First-pass proof read up to here*

## 1.4 Magnetic Braking

*Fill in some more stuff. You have some points in the "problems with modelling" bit later.*

Consider a blob of this charged wind material, moving with some sideways velocity in the plane of the orbit, almost certainly slower than the magnetic field lines. The blob will interact with the field and accelerated to co-rotate with them. This higher velocity causes it to move outwards, to a higher orbit, where the field lines are moving even faster, accelerating the blob more. The wind then robs the star associated with the magnetic field of rotational angular momentum and its spin rate is slowed. The close proximity of the binary means that tidal effects are strong, and the donor is spun up again by robbing the orbit of angular momentum, reducing their separation and hardening the binary further (Verbunt & Zwaan, 1981).

As an aside, Wickramasinghe et al. (1996) presented theoretical motivation that CVs can have too strong a magnetic field to allow magnetic braking. Open field lines are necessary for wind to escape the system, so too strong a white dwarf magnetic field can trap the ionised gas in-system, suppressing the wind of the secondary. This Magnetic CV subclass is briefly described in §1.8.1.

As the magnetic braking mechanism is a direct consequence of the donor star spinning down, the CV community is able to borrow insights from adjacent fields of study. The majority of M dwarfs experience some form of spin-down under magnetic braking , so observations of the magnetic field strengths of singletons *cite this* should inform the efficacy of magnetic braking in CV binaries. Unfortunately, *cite this* the typical CV rotational period is on the order of a few hours, and singleton M

dwarfs are considered extremely fast rotators with periods of a day. Observations [cite this] of singletons simply do not reach to the extremely low mass, rapid rotations that are frequently seen in CVs, so we are forced to rely on extrapolation and theory.

This carries with it some major practical issues. One is that while the broad effects of magnetic fields is relatively easy to intuit, quantitative physical understanding the mechanics and origins of magnetic fields is difficult, involving fluid dynamics, considering interactions with the accretion disc, and magnetism acting on large systems, which quickly become prohibitive to model and is usually handled with one of a variety of recipes. Knigge et al. 2011 contains a detailed compilation of some older approaches, but the decade since has seen a few newer methodologies emerge. Here, two recent magnetic braking prescriptions are described in moderate detail: the Matt et al. (2015) prescription, and the Garraffo et al. (2018a) prescription. For a more complete, detailed summary of the modern understanding of M dwarf magnetic fields refer to Kochukhov (2021).

## 1.4.1 Matt prescription for magnetic torque

In Matt et al. (2015), an empirical prescription is derived that relates the torque felt by a low mass main sequence star to that stars' mass, radius, and Rossby number. The Rossby number is a fluid dynamics term for the ratio between the inertial and Coriolis force terms of the Navier-Stokes equations. A small Rossby number indicates a system dominated by Coriolis effects, and a large Rossby number indicates that centrifugal and inertial forces dominate. The Rossby number of a main sequence star can be calculated from $\Omega$, it's angular rotation rate, and $\tau_{\mathrm{cz}}$, the convective turnover timescale.

$$\mathrm{Ro} = (\Omega \cdot \tau_{\mathrm{cz}})^{-1} \tag{1.10}$$

Through the Rossby number, the effectiveness of magnetic braking is tied to rotation, which is extremely fast in CVs, and stellar mass and age, which affect $\tau_{\mathrm{cz}}$.

Their work makes use of observations of stars with masses less than $0.15 - 1.3 M_\odot$ and span ages of $\sim 10^{6-9}$ yrs, that have had their rotation periods measured. This dataset is used to calibrate a theoretically motivated empirical prescription for magnetic braking. There is some evidence for a saturation of magnetic activity below a critical Rossby value (a.k.a. above a critical rotational pe-

riod) (Reiners et al., 2009), where magnetic activity seems to no longer respond to changes in rotation. Matt et al. (2015) adopt two generic relationships,

$$\left(\frac{B_*}{B_\odot}\right)^{4m}\left(\frac{\dot{M}_\omega}{\dot{M}_\odot}\right)^{1-2m} = Q\left(\frac{\text{Ro}_\odot}{\text{Ro}}\right)^p \tag{1.11}$$

in the unsaturated regime, and

$$\left(\frac{B_*}{B_\odot}\right)^{4m}\left(\frac{\dot{M}_\omega}{\dot{M}_\odot}\right)^{1-2m} = Q\chi^p \tag{1.12}$$

in the saturated regime. Here, $M_*$ and $R_*$ are the stellar mass and radius, $B_*$ is the magnetic field strength at the stellar surface, and $M_\omega$ is the total mass outflow rate. The $m$ exponent is determined by the field geometry and wind acceleration profile, but functionally is a tuning parameter that likely falls in the range of $0.20 < m < 0.25$ (Matt et al., 2015). The $p$ exponent encodes the dependence of magnetism on the Rossby number, $Ro$, and is assigned as $p = 2$. $\chi$ is the inverse critical Rossby number for saturation, for which Matt et al. (2015) adopt a value of 10. $Q$ is a generic scale factor that the authors fit to observations.

The authors use these equations to eventually derive the spin rates for main sequence stars at some time $t$ after their initial spin period, $\Omega_i$,

$$\lim_{\Omega_* \gg \Omega_{\text{sat}}} \left(\frac{\Omega_*}{\Omega_\odot}\right) \to \left(\frac{\tau_{\text{unsat}}}{t}\right)^{\frac{1}{p}} \tag{1.13}$$

$$\Omega_* = \Omega_i \cdot e^{-t/\tau_{\text{sat}}} \tag{1.14}$$

for a rotation period of $\Omega_*$, and the threshold for saturation at $\Omega_{\text{sat}}$. The two $\tau$ factors, $\tau_{\text{sat}}$ and $\tau_{\text{unsat}}$, are the spin-down timescales in the saturated and unsaturated regimes, and $\tau_{\text{sat}} \ll \tau_{\text{unsat}}$.

The authors take observations of two clusters, the $\sim 5$ Myr old ONC cluster and the $\sim 580$ Myr old Praesepe cluster, and use the first as initial conditions and the second as target distribution to reproduce. Figure 1.3 is taken from Matt et al. (2015), and compares the initial and final conditions of their synthetic cluster model compared to these two boundary conditions. During the first few tens of Myrs of this model, the stars in the synthetic cluster are spun up as they contract, lowering their periods by factors of $\sim 5 - 10$. After this initial phase, which is much shorter than the spin down timescales, the more long-term spin
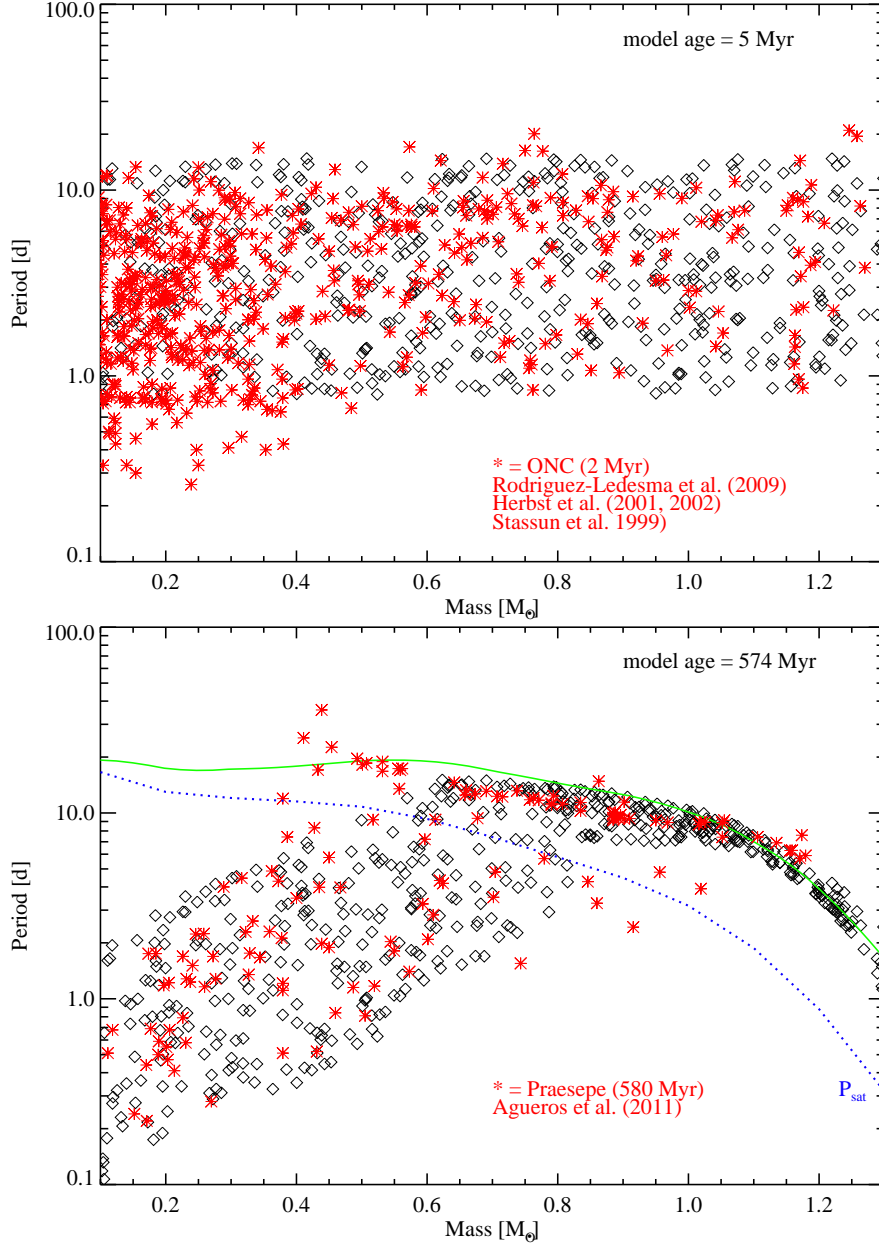
Figure 1.3: Figure taken from Matt et al. (2015). Red crosses are observations of the ONC (*top*) and Praesepe (*bottom*) cluster stars. Black diamonds are synthetic cluster stars. In the bottom panel, the solid green line is the theoretical asymptotic spin rate of unsaturated stars and the dotted blue line delimits magnetically saturated and unsaturated stars.

evolution begins.

The agreement between the synthetic cluster and the Praesepe cluster at 574 Mrys is impressive. Above $\sim 0.8 M_\odot$, stars converge on a single narrow mass - period track just as is seen in the observations, and the large scatter below

$\sim 0.8 M_\odot$ is also reproduced. Also, just as is seen in the cluster observations of Praesepe, the fastest rotators are those with the lowest masses. Both of these features arise from the transition from saturated braking, to unsaturated braking (Matt et al., 2015).

At formation, almost all stars are experiencing saturated magnetic braking. The single narrow track arises from higher mass stars spinning down faster than lower mass stars, bringing them down to the much less efficient unsaturated braking regime sooner. The pile-up of systems then produces the narrow track. The mass dependancy of this track comes from the fact that $\tau_{unsat}$ is shorter for lower mass stars. The broad population of low mass rapid rotators is a direct result of the broad initial conditions, which span an order of magnitude themselves, and the longer spin-down time of lower mass stars in the saturated regime allowing them to remain at high rotation rates for longer.

However, this model does fail in a few key respects. In the right panel of Figure 1.3, a small population of very slow rotators can be seen at $\sim 0.4 M_\odot$. The slower rotation rates of these stars suggests an alternative spin-down mechanism. The inverse problem is seel at $\sim 0.7 M_\odot$, where a handful of stars are seen rotating *faster* than predicted by any of the synthetic cluster stars, suggesting that magnetic braking is not as effective in their case. More importantly for the CV field, the parameter space of CVs is completely uncovered, as CVs have rotation periods of $< 0.2$ days on the high end, and the systems that this work concerns have periods of $\lesssim 0.07$ days. While this would firmly place CVs in the saturated regime, there is evidence of a 'supersaturated' regime at extreme rotation periods that may be relevant to CV donors (James et al., 2000; Wright et al., 2011; Argiroffi et al., 2016). This possibility is also noted by Gossage et al. (2021) when outlining best practice use of this prescription in the stellar evolution code MESA, though the subject is not a settled matter and competing evidence for the *lack* of supersaturation has been reported by Jeffries et al. (2011).

## 1.4.2 Garraffo prescription for magnetic torque

The Garraffo et al. (2018a) model considers the morphology of the magnetic field to also be important the the strength of magnetic braking, based on the work by Garraffo et al. (2015). The primary justification for this inclusion is observations of open clusters of a known age, where a bimodality is seen in the rotation rates of stars of similar masses. Some stars appear to be fast rotators, and some are slow

Cite skumanich gap

rotators, and there is a dearth of systems between the two. Previous attempts to model this bimodality have relied on a random, unexplained transition between an efficient braking state, and an inefficient braking state (Spada et al., 2011; Reiners & Mohanty, 2012; Gallet & Bouvier, 2013), and Garraffo et al. (2018a) expand on this by offering a shift in magnetic field morphology as the underlying trigger.

Their formalisation of this is based on two assumptions. They assume that stars with the dipolar component of the magnetic field dominating follow a known spin-down law, with a mass dependence reflecting $\tau_{\mathrm{cz}}$. Second, they assume that there is some relationship between field morphology and stellar spin rate. Specifically, that stars rotating more rapidly have more complex magnetic fields. This is formalised via an AML rate, $\dot{J}$,

$$\dot{J} = \dot{J}_{\mathrm{dipole}} Q_J(n) \qquad (1.15)$$

where $\dot{J}_{\mathrm{dipole}}$ is the dipole loss under the Skumanich law, $\dot{J}_{\mathrm{dipole}} \propto \Omega^3 \tau$. $Q_J$ is a modulating factor that encapsulates the field complexity at the stellar surface, and is controlled by the complexity factor, $n$, which has its own prescription (Garraffo et al., 2016).

$$Q_J(n) = 4.05 e^{-1.4n} + \frac{n-1}{60Bn} \qquad (1.16)$$

Where $B$ is the magnetic field strength at the stellar surface. As the second term is only significant for $n > 7$, Garraffo et al. (2018a) consider only the first term of this relation. This is the equivalent of the saturation of magnetic braking from §1.4.1, but here is contingent on field complexity rather than Ro.

Garraffo et al. (2018a) suggest the following relation between Ro and $n$,

$$n = 1 + \frac{0.02}{\mathrm{Ro}} + 2\mathrm{Ro} \qquad (1.17)$$

based on observations of open clusters. The three terms reflect three aspects of the magnetic braking model - the minimum complexity is defined as $n \equiv 1$, the first factor encodes stars with small Ro having large $n$ (e.g. young, fast rotators), and the third term gives stars with large Ro similarly large $n$. This prescription means that the AML of a star is purely a function of its Rossby number, c.f. Equation 1.10.

cite Skumanich
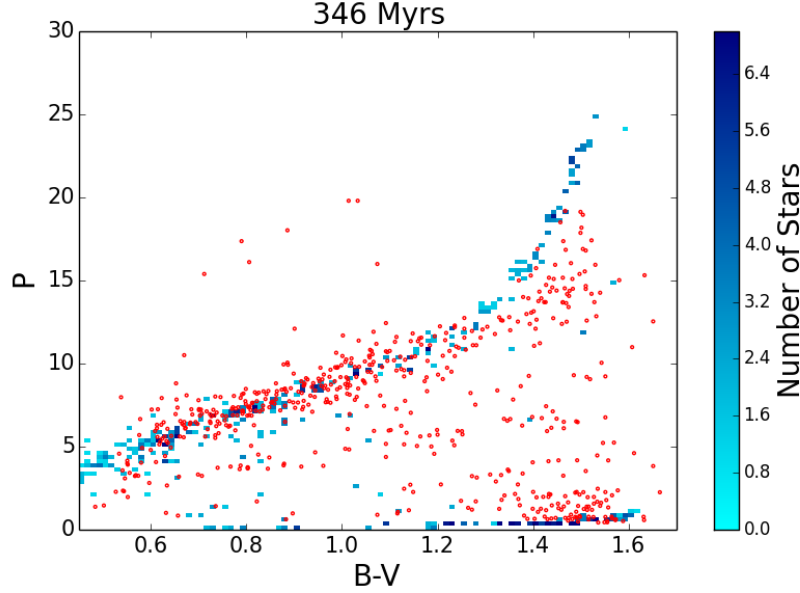
Figure 1.4: Example comparison between synthetic and observed cluster populations taken from Garraffo et al. (2018a). Red points are observations of M37, which has its age measured at $\sim 346 - 550$ Myrs. Blue points are the probability distribution of the synthetic cluster population from Garraffo et al. (2018a).

Similarly to Matt et al. (2015), Garraffo et al. (2018a) run a population synthesis model to compare to observations using initial conditions taken from the 13 Myr old h Persei cluster (Moraux et al., 2013), but the authors show that differences between alternative initial conditions do not survive longer than 200 Myrs. Observations of stellar rotation periods and colour from several clusters with known ages are then compared to the synthetic population.

The resulting distribution does recover the Skumanich bifurcation observed in open clusters, reproducing the fast and slow rotating populations and the gap between them, though the large uncertainty in the age of the cluster does introduce some discrepancy. In addition, the synthetic cluster does not consider the effects of close binary stars, which will affect the spin-down rate through tidal effects. As the comparison to data is done with color, filtering out binaries is difficult. However, this effect is ignored by the author, as there is evidence that the binary fraction in open clusters is low (Meibom et al., 2007). The mass dependency of this track is also reproduced by the model, and Figure 1.4.

The Garraffo et al. (2018a) prescription is simpler in concept than the Matt et al. (2015) prescription, and both prescriptions perform well. However, neither formulation covers the parameter space of CV donors, and both are semi-empirical with some arbitrary decisions made in order to fit data. This makes both approaches highly vulnerable to extrapolation errors and difficult to trust in the context of CV evolution, especially in the short period regime.

## 1.5    Accretion in CVs

Accretion physics is important to the appearance and behaviour of a CV. While it is summarised here, more in-depth descriptions can be found in Warner (1995); Hellier (2001); Ritter (2010b).

When the donor star overfills its Roche lobe, matter is ejected from its surface at thermal velocities – $\sim 10$km s$^{-1}$ for a 5000K M dwarf. This is small when compared to the orbital velocity of the system, and M dwarf velocities of $\sim 400 - 500$ kms$^{-1}$ are common in the observations reported in §. Since the ejected material is effectively stationary as it leaves the donor, it falls along a ballistic trajectory towards the white dwarf primary and forms an accretion disc around it.

> Put this section in!

Disc material gradually loses angular momentum and gravitational potential energy due to its viscosity, which acts over time to concentrate the majority of the disc's angular momentum in the minority of the disc's mass, ejecting some material at high velocities at the expense of moving the remainder closer to the white dwarf. This viscosity partially arises from friction within the fluid of the disc but the main source is thought to be from turbulence, random eddy currents moving material to different radii. This form of turbulence in a thin disc was formalised in the alpha disc model by Shakura & Sunyaev (1973), where viscosity, $\nu$, is related to scale height, $H$, and the speed of sound, $c_s$, by a free parameter, $\alpha$.

$$\nu = \alpha c_s H \tag{1.18}$$

Since turbulent eddies cannot be larger than $H$ or have velocities greater than $c_s$, $c_s H$ forms the upper limit of $\nu$, and $\alpha$ is limited in this model to values between 0 and 1. In typical CV accretion discs (i.e. quiescent discs, see §1.8.4), $\alpha$ takes values from $\sim 0.01 - 0.05$ Hellier (2001).

Material that enters the disc must lose gravitational potential energy before it

can be accreted to the white dwarf surface. Approximately half of this energy is lost thermally, through radiating accretion light, and the other half is converted to the kinetic energy necessary to maintain orbit about the white dwarf at lower altitudes. This low orbit has typical velocities roughly an order of magnitude higher than the rotational velocity of the white dwarf, so for material to settle on the stars' surface it must dissipate a large amount of kinetic energy. A region between the inner edge of the disc, and the surface of the white dwarf where this deceleration occurs is called the boundary layer, and can be a significant contributor to the total brightness of a CV.

As the white dwarf is accreting material to its surface, one might expect it to grow in mass over time, and possibly even detonate as a Ia supernova as it crosses the $1.4 M_\odot$ Chandrasekhar limit. This postulation is supported by the white dwarfs in CVs being significantly more massive than their singleton counterparts , but were this the case we would expect there to be a relationship between age, `ref` and white dwarf mass. McAllister et al. (2019) searched for this relationship, but found no correlation between the two, indicating that the white dwarfs in CVs do not grow over time, and are unlikely to reach the Chandrasekhar limit. Growth is thought to be limited by the accreted material cyclically detonating, in events called Classical Novae, outlined in §1.8.3 (Wijnen et al., 2015; Sparks & Sion, 2021). Indeed, this serial detonation is invoked as a potential source of AML, dubbed Consequential AML (CAML), that is described in §1.6.3.

## 1.6  A modern understanding of AML

A solid knowledge of exactly how and why CVs lose angular momentum has remained surprisingly elusive for several decades now. Early theories established gravitational waves and magnetic braking as the only two sources of AML , but at- `ref` tempts to quantify this with evolutionary models and population synthesis models `ref` consistently fall short, as outlined in §1.3.1. Gravitational losses are well under- `ref` stood, and have been independently observed and studied, but the sources and consequences of magnetism in a stellar context is not so easy. CVs provide a testbed for probing magnetism in low mass stars that will be useful in other contexts.

The missing source of AML is not necessarily magnetic in nature.

Here are some links to papers that I should reference here.

- Evidence for reduced magnetic braking

- THE INFLUENCE OF NOVA ERUPTIONS

- eCAML paper, schrieber 2016

- Nova-produced Common Envelope: Source of the Nonsolar Abundances and an Additional Frictional Angular Momentum Loss in Cataclysmic Variables

- The origin of magnetic fields in CV white dwarfs (2020)

### 1.6.1 The missing AML problem

See the first year literature review for some content here. This subsection should quantify the missing AML problem with real observations and models, and tee up the next parts where some proposed solutions are discussed.

### 1.6.2 Residual magnetic braking

### 1.6.3 Consequential AML

also talk about empirical CAML, eCAML, here (Schreiber et al., 2016).

This will be very important! Lower mass donors will be able to accrete and retain less nova-processed material, so more will be lost from the system and carry with it more angular momentum. I think this dovetails with the lower mass white dwarf correlating with higher excess AML, since the same logic applies - the lower escape velocity from the system should allow more material to carry away angular momentum. (https://ui.adsabs.harvard.edu/abs/2021ApJ...914....5S/abstract)

## 1.7 Further issues with established CV models

Population studies expect that up to 50% of CVs should host a helium white dwarf (Politano, 1996), though to date this has been notoriously difficult to test. Zorotovic & Schreiber (2010) examined a sample of post-common envelope binaries and found only $13 \pm 7\%$ of the sample to be expected to evolve into a CV containing a helium white dwarf. On the white dwarf mass problem of CVs

Additionally, observation and theory disagree on the white dwarf mass produced in CV evolution (Wijnen et al., 2015; Liu & Li, 2016; Parsons et al., 2017),

with models predicting an excess of low-mass white dwarfs that are not observed. On top of this, there is the question of "do CVs grow in mass over time as they accrete?", to which the answer is no.

Also, we expect there to be about 13% of systems forming with a brown dwarf, which would put them below the period minimum – which is not observed.

Ritter has some good points that I should include

## 1.8 CV variability and subtypes

is this ok?

The sections above have outlined the general structure and evolution of a CV, but not all systems are well described by this picture. CVs exhibit significant variability even on human timescales, often on the order of several magnitudes in brightness. Further, a few subtypes of CV exist that either lie significantly outside the normal evolutionary tracks we expect, or contain exotic components. These are briefly discussed, though the focus of this work is on "classic" CVs, and the majority of these subtypes are fundamentally incompatible with our analysis techniques.

### 1.8.1 Magnetic CVs

It is possible for white dwarfs to have very strong magnetic fields, in the region of tens to hundreds of megagauss. Such white dwarfs are called polars, and are an interesting field of study in their own right, but when a polar is accreting material from a donor star the system is designated as an AM Her star. The intense magnetic field strength alters the CV evolution in a two main ways. The strong field lines of the polar mean that the hot, charged photosphere material transferred to the primary cannot form an accretion disc and instead falls directly onto the surface of the white dwarf. The impacting material forms a bright spot on its surface, which is usually bright enough to be visible from earth. In addition, the strong field lines force the white dwarf to become tidally locked to the donor star.

There is also a subclass of magnetic CVs with weaker field strengths of a few megagauss, known as DQ Her stars. In these systems, the white dwarf is not tidally locked, and a partial disc can exist. However, as the existence of a disc is crucial to the characterisation technique used in this work (see §WHAT for details), magnetic CVs are unsuitable for our analysis.

Put in the relevant section here

## 1.8.2 Helium-rich CVs

A small number of CV donors are helium-rich, with much smaller radii than their hydrogen-rich counterparts; these can be semi-degenerate helium stars, the cores of highly evolved main sequence stars, or a second white dwarf. The As a CV donor must be in contact with its Roche lobe, such systems are far more compact than usual, with orbital periods $\lesssim 65$ minutes. Such systems are AM CVn stars, after the prototypical system AM Canum Venaticorum. For further discussion on AM CVn stars, see (Solheim, 2010).

## 1.8.3 Classical Novae

The white dwarf in a CV is almost constantly accreting matter onto its surface. Over time this surface layer can build up, and get placed under immense pressure by the gravity of the white dwarf. Eventually, pressures rise enough to force material at the boundary to become degenerate, and once hot enough this boundary layer can begin nuclear fusion. Since the accreted material has become degenerate, it cannot expand in response to the extra energy from fusion and simply heats further, leading to more and more fusion and culminating in a complete detonation of the accreted material on the white dwarf's surface (Warner, 1995). This detonation is finally able to overcome the surface gravity of the white dwarf, and the accreted material is blown from the surface. These are generally one-off events, recognised by a significant brightening of the system of between 6 and 19 magnitudes, lasting anywhere from a few days, so several months.

Once a system has experienced a classical nova, it is classified as a CNe system. (Warner, 1995). However, theory suggests that all CVs experience classical novae many times over their lifetimes. The required amount of accreted material for the nova to occur depends on mass, but lies between $3 \times 10^{-5} M_{\odot}$ of hydrogen for a $1.3 M_{\odot}$ white dwarf, and $5 \times 10^{-3} M_{\odot}$ for a low mass, $0.6 M_{\odot}$ white dwarf (Hellier, 2001). Typical CV accretion rates are around $10^{-9} M_{\odot} \ yr^{-1}$ for long period systems, and $10^{-10} M_{\odot} \ yr^{-1}$ for short period systems (Hellier, 2001; Pala et al., 2021), suggesting classical novae recur at most every few million years, down to every few tens of thousands of years.

The amount of material retained by the white dwarf is likely negligible. Both population synthesis by (Wijnen et al., 2015) and observations by (McAllister et al., 2017) indicate no evidence of mass growth over time for the white dwarfs

in CVs, and hence that the expulsion of the accreted material in a classical nova is complete.

A final note is that some CVs show multiple classical novae in relatively quick succession (Schaefer, 2010). These Recurrent Novae (RNe) are distinguished by having more than one observed nova event recorded. As good quality data only exist for the last few centuries, this enforces a soft limit on recurrence interval of a few hundred years, though recent efforts have been made to search ancient records for candidate events (Hoffmann & Vogt, 2022). Only a handful of confirmed RNe are known; the variable star index (Watson et al., 2006) only contains 11 systems classified as RNe.

### 1.8.4   Dwarf Novae

CVs also undergo less extreme brightening events, called Dwarf Nova (DN) outbursts. These brighten the system by between 2 and 5 magnitudes (Warner, 1995) and are more brief than typical CNe, lasting less than $\sim 20$ days. However, in contrast to CNe, they have recurrence times much more in line with human timescales, ranging from a few days to some decades. This is due to the fundamental difference in the physical origin of the two phenomena.

DN outbursts do not originate directly from either star in the system, but rather from the accretion disc around the white dwarf. Such outbursts are well-described by the disc instability model (Cannizzo, 1993; Dubus et al., 2018).

Initially, the disc is in a cooler, "low" state with low temperature, low surface density, and low viscosity. Material in the disc moves inwards due to friction from turbulence (see §1.5) which is relatively weak in the low viscosity material, so radial movement of disc material is slow.

If the accretion rate of donor material exceeds the rate material falls onto the surface of the white dwarf, then a buildup of matter begins in the disc, raising the density and temperature. Eventually, this annulus reaches $\sim 7000K$, at which point hydrogen becomes partially ionised and a rapid further increase in temperature is triggered as the material becomes optically thick and heat is trapped in the disc. In addition, as the temperature and density rise, so does $c_s$, and following Equation 1.18, so does viscosity, even assuming constant $\alpha$. In fact, $\alpha$ *rises* during outburst, to $\alpha \sim 0.1 - 0.5$ (Hellier, 2001). This hot, luminous, "high" state is again stable, and the disc is said to be in outburst. Now that the disc is more viscous, material is moved inwards more readily. The infall

Unsure if I should talk about the outburst starting in an annulus, and spreading outwards from there? Seems unnecessary

rate onto the white dwarf is much increased, and is now higher than the mass transfer rate, so the disc is drained onto the surface of the white dwarf. As it does so, the surface density and temperature begin to fall, and eventually protons and electrons recombine into hydrogen. While recombination is an exothermic process, the release of energy is outweighed by the material once again becoming optically thin and allowing radiation to more easily escape the disc. The disc now quickly cools back down to the quiescent, "low" state, returning to a low surface density, and the cycle can repeat itself. For a more in-depth look at this model, refer to discussions by Cannizzo (1993), Osaki (1996), Warner (1995), (Hellier, 2001), and Hameury (2002).

Three types of DNe exist, which exhibit somewhat different behaviour than what is outlined above. The first of which are SS Cyg stars, distinguished by very consistent amplitudes across outbursts, though there is variation in length, shape, and recurrence time.

Z Cam stars exhibit standstills, events where the system enters outburst, peaks in brightness, then begins to dim. However, rather than returning to its quiescent magnitude, the brightness is maintained $\sim 1 - 1.5$ magnitudes below peak brightness for a long period of time, typically between a few days, and a few years (Simonsen et al., 2014).

The third subtype are SU UMa stars. These systems are known for their more complex behaviour, exhibiting superoutbursts and superhumping, and are described in §1.8.5

## 1.8.5 SU UMa stars

SU UMa stars are distinguished by exhibiting superoutbursts, similar to the regular outbursts that the star still undergoes, but with greater amplitudes and durations, but longer recurrence times. These outbursts are triggered by the disc radius growing to such an extent that it becomes tidally perturbed by the donor star, and turns elliptical. This can only take place for when the donor star is less than $\sim 1/3$ the white dwarf mass, so only short period systems see these superoutbursts. (Hellier, 2001). SU UMa stars are also known for their superhumping, which also arises from the disc eccentricity. The tidal interaction between the disc and the donor produces an area of increased luminosity at the edge of the disc between the white dwarf and the donor (Warner & O'Donoghue, 1988). As the disc is elliptical, the distance between this disc edge and the donor varies

over the course of an orbit, causing a similar variation in brightness as the donor moves around the disc. These fluctuations are called superhumps, and are useful as they provide a diagnostic to the mass ratio for the system as the (Patterson, 1998, 2001; Patterson et al., 2005). Because of the strong influence of the donor, the disc is also subject to precession, with a precession rate slightly longer than the orbital period. The superhump period, $P_{\mathrm{hump}}$ is then a combination of the orbital period, $P_{\mathrm{orb}}$, and the precessional period $P_{\mathrm{pr}}$,

$$\frac{1}{P_{\mathrm{hump}}} = \frac{1}{P_{\mathrm{orb}}} - \frac{1}{P_{\mathrm{pr}}} \tag{1.19}$$

and can be readily observed with photometry from earth without the need for precise alignment that eclipse modelling requires. Since the precession period is dependant on the mass ratio and the disc radius, by finding the superhumping period of eclipsing CVs an empirical relationship can be found between the superhumping excess, $\epsilon$, and the mass ratio of a CV, where:

$$\epsilon = \frac{P_{\mathrm{hump}} - P_{\mathrm{orb}}}{P_{\mathrm{orb}}} \tag{1.20}$$

and several papers exist discussing and calibrating this relationship, see McAllister et al. (2019) for a recent calibration and good starting point for more information.

### 1.8.6   Nova-like systems

The disc instability model applies to CVs with mass transfer rates that are high enough to exceed the infall rate onto the CV during the "low" state, but low enough that the "high" state can still empty the disc. However, a subset of CVs have mass transfer rates high enough to sustain the high state and maintain a permanent outburst mode. Such systems are called Novalikes, or NL systems. Most NL CVs show little to no brightness variation, though a small number known as VY Scl stars do occasionally enter "low" states and dip in brightness by several magnitudes. Livio & Pringle (1994) propose that this is triggered by a starspot rotating into the L1 point causing a fall in mass transfer rate. A precise mechanism here is not given, but since star spots are regions of concentrated magnetic fields, it is postulated that the stronger magnetic field of the spot disrupts magnetic braking in some fashion. A competing theory from Wu et al. (1995) proposes that the fall in brightness is caused by the irradiation of the donor stars' atmosphere

driving mass transfer, and that when this irradiation becomes blocked, the mass transfer rate falls enough for the disc to enter the low state for a short time.

## 1.9 Probing CV evolution

The technique used for this thesis is primarily eclipse modelling, and MESA stellar evolution modelling, both of which are explained in detail in Chapter 3

### 1.9.1 $\epsilon - q$ relation for superhumpers

### 1.9.2 Donor mass-radius relation

> Essentially, Knigge 2011

### 1.9.3 Spectroscopy of the white dwarf

> Pala 2021 should be talked about here, along with whatever else you can dig up about spectroscopic analysis.

## 1.10 Closing remarks, and recap

# Chapter 2

# Observations and observational techniques

For CVs with a sufficiently high inclination ($\gtrsim 80$ deg, depending on mass ratio) the donor will eclipse all other components of the system in quick succession, once per orbit. Observing and modelling these eclipses, with knowledge of the orbital period and the temperature of the white dwarf, can lead to a thorough characterisation of the CV. The methodology for this characterisation is described in detail in §3, but essentially relies on extracting the white dwarf temperature and radius from the white dwarf colours, and using the timing of eclipse features to find the component masses, donor radius, and orbital separation.

The work of this thesis has made extensive use of three instruments: ULTRACAM, HiPERCAM, and ULTRASPEC . These are time-series photometric imaging instruments, capable of taking high-cadence images of the night sky in one, three, or five colours, respectively. Crucially, HiPERCAM and ULTRACAM make their multi-colour images simultaneously, which is later very important to the modelling technique used to characterise our CV systems. The eclipses we observe typically span less than 30 minutes, and the instruments must be sensitive to changes on the order of a few seconds to be useful for analysis, and these three cameras are ideal for this task.

> Cite the instrument papers!

## 2.1 HiPERCAM

## 2.2 ULTRACAM

## 2.3 ULTRASPEC

## 2.4 Data reduction

### 2.4.1 The HiPERCAM pipeline

**Bias frames**

**Flat fielding**

**Aperture photometry**

> Talk about the pipeline on a high level here. Outline how a reduction config file is made that encapsulates the reduction settings, and embeds these settings in the final output

Table 2.1: Atmospheric extinction coefficients for La Silla, derived from ULTRA-CAM/NTT observations.

| Date of Observation | Airmass Range | Band | $k_{ext}$ |
|---|---|---|---|
| 14 Oct 2018 | 1.30-1.98 | $u_{\text{reg}}$ | 0.4476 |
| | | $g_{\text{reg}}$ | 0.1776 |
| | | $r_{\text{reg}}$ | 0.0861 |
| 30 Sept 2019 | 1.03-1.63 | $u_{\text{sup}}$ | 0.4867 |
| | | $g_{\text{sup}}$ | 0.1803 |
| | | $r_{\text{sup}}$ | 0.0713 |

## 2.5 Photometric calibration

For all observational data contained in this thesis, the HiPERCAM data reduction pipeline (Dhillon et al., 2016) was used to perform debiassing and flat-field corrections on the raw frames, as described in §2.4. The software was also used for the extraction of aperture photometery, producing the flux in Analog-to-Digital Units, ADU, per frame of each source. A comparison star in the same image as the target was used to account for transparency variations, and standard stars from Smith et al. (2002) were used to transform the lightcurves from ADU to the SDSS $u'g'r'i'z'$ photometric system.

### 2.5.1 Calculating atmospheric extinction coefficients

Atmospheric extinction was calculated using the longest continuous ULTRACAM observation available within 3 days of the target observations. The atmospheric extinction values are reported in Table 2.1. For dates where no observations spanned a satisfactory range of airmasses, the nearest observation in time was used as a stand-in, as atmospheric extinction coefficients are usually relatively stable over time. Aperture photometery was extracted for five sources in these long observations, and the instrumental magnitude, $m_{\text{inst}}$, vs airmass, $\chi$, was fit with a straight line for each source. The gradients of these lines are the atmospheric extinction coefficients, $k_{\text{ext}}$, for the relevant band, and the y-intercept is the instrumental magnitude of that object above the atmosphere, $m_{\text{inst,0}}$:

$$m_{\text{inst}} = m_{\text{inst,0}} + \chi k_{\text{ext}}$$

Currently, this is only for a very narrow range of the actual observations. Generalise this table to include all instruments and locations.

## 2.5.2   Transformations between filter systems

The ULTRACAM photometric system previously matched the SDSS reasonably closely, however in early 2019 it was upgraded and now uses an SDSS-*like* filter system with higher efficiency bandpasses, referred to as Super SDSS. There are three optical paths that are relevant:

- SDSS filters, $u', g', r', i', z'$;

- ULTRACAM SDSS, NTT, $u_{\mathrm{reg}}, g_{\mathrm{reg}}, r_{\mathrm{reg}}, i_{\mathrm{reg}}, z_{\mathrm{reg}}$;

- ULTRACAM Super SDSS, NTT, $u_{\mathrm{sup}}, g_{\mathrm{sup}}, r_{\mathrm{sup}}, i_{\mathrm{sup}}, z_{\mathrm{sup}}$.

We aim to place our photometery in the SDSS $u'g'r'i'z'$ system, as this is the system later used by the white dwarf atmospheric models. The $u_{\mathrm{reg}}, g_{\mathrm{reg}}, r_{\mathrm{reg}}, i_{\mathrm{reg}}$ filters were sufficiently similar to standard SDSS filters that the uncorrected magnitudes of standard reference stars from Smith et al. (2002) could be used to calibrate absolute photometry without issue. However, with the new filters, there was concern that the different shape of the sensitivity curve, particularly in the $u'$ band, differ enough from the standard filters to cause issues with our photometric calibration. Figure 2.1 illustrates the change in throughput between the SDSS photometric system, and the Super SDSS filters, on ULTRACAM on the NTT.

To perform the colour corrections, the following equation for the magnitude of a star was used, using the $g'$ band as an example:

$$g' = g_{\mathrm{inst}} + \chi k_{\mathrm{ext}} + g_{\mathrm{zp}} + c_{\mathrm{g,sup}}(g' - r') \tag{2.1}$$

where $g_{\mathrm{zp}}$ is the zero point, $g_{\mathrm{inst}} = -2.5\log(\mathrm{ADU}/t_{\mathrm{exp}})$ for an exposure time of $t_{\mathrm{exp}}$, and $c_{\mathrm{g,sup}}$ is the colour term correction gradient.

The optical path of each system was simulated using the `pysynphot` package, with measured throughputs of all ULTRACAM components in the optical path. Models from Dotter (2016) and Choi et al. (2016) were used to generate the $T_{\mathrm{eff}}$ and log(g) values of an 8.5 Gyr isochrone for main sequence stars with masses from 0.1 to 3 $M_\odot$. These span from log(g)= 3.73 $\rightarrow$ 5.17, and $T_{\mathrm{eff}} = 2900\mathrm{K} \rightarrow 10,300\mathrm{K}$. The Phoenix model atmospheres (Allard et al., 2012) were used to generate model spectra of each mass, which was then folded through each optical path to calculate an AB magnitude. In addition, white dwarf models with log(g)=
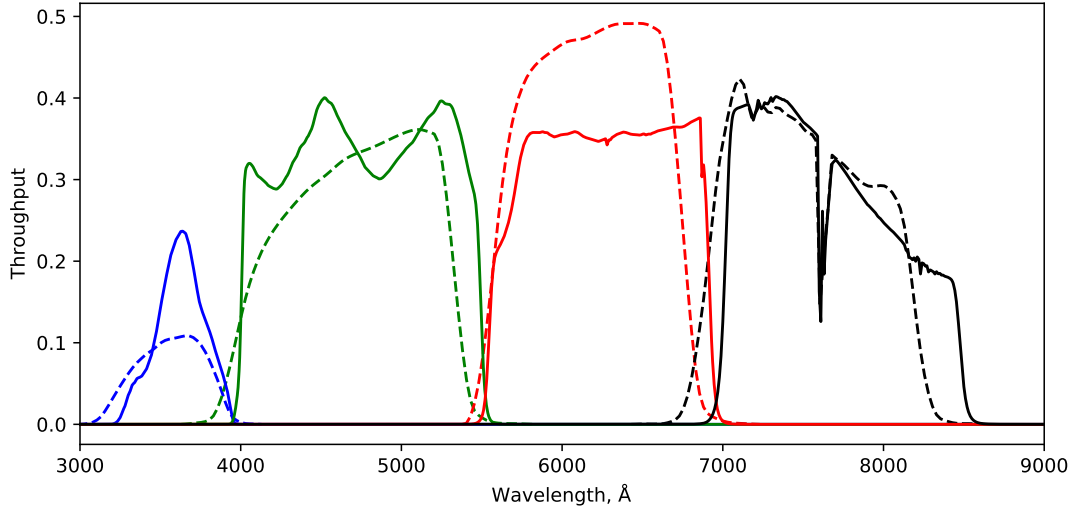
Figure 2.1: The differences in photometric throughput for SDSS filter system (dotted lines), and ULTRACAM Super SDSS filters, for ULTRACAM mounted on the NTT (solid lines). Blue: $u$ bands, Green: $g$ bands, Red: $r$ bands, Black: $i$ bands. Both throughputs include atmospheric extinction of $\chi = 1.3$.

8.5 were similarly processed (Koester, 2010; Tremblay & Bergeron, 2009), to asses the impact of the different spectral shape on the resulting colour terms.

We synthesised the colour terms between the SDSS and ULTRACAM Super SDSS systems, e.g., $g' - g_{\mathrm{sup}}$, for each model atmosphere. These data were plotted against SDSS colours, i.e. $(u' - g')$, $(g' - r')$, $(g' - i')$, and a straight line was fit to the colour relationship. In the example case of $g' - g_{\mathrm{sup}}$, this would be

$$g' = g_{\mathrm{sup}} + g_{\mathrm{zp}} + c_{\mathrm{g,sup}}(g' - r')$$

Note we ignore the effects of secondary extinction. These relationships are shown in Figure 2.2 for all four ULTRACAM filters used to observe these CVs, and Table 2.2 contains the coefficients of each colour term. $(u' - g')$ was used to correct $u$ magnitudes, $(g' - r')$ was used to correct $g$ and $r$ magnitudes, $(g' - i')$ was used to correct the $i$ band. These colour corrections are not generally the same for main sequence stars and white dwarfs, though the colours of the white dwarfs presented in this work are all such that the discrepancy is on the order of a few percent, and is considered negligible.

Table 2.2: Colour term best fit lines from Figure 2.2. The data are modelled by equations of the form $(u' - u_s) = \phi + c_u(u' - g')$, with $c_u$ being the relevant colour gradient.

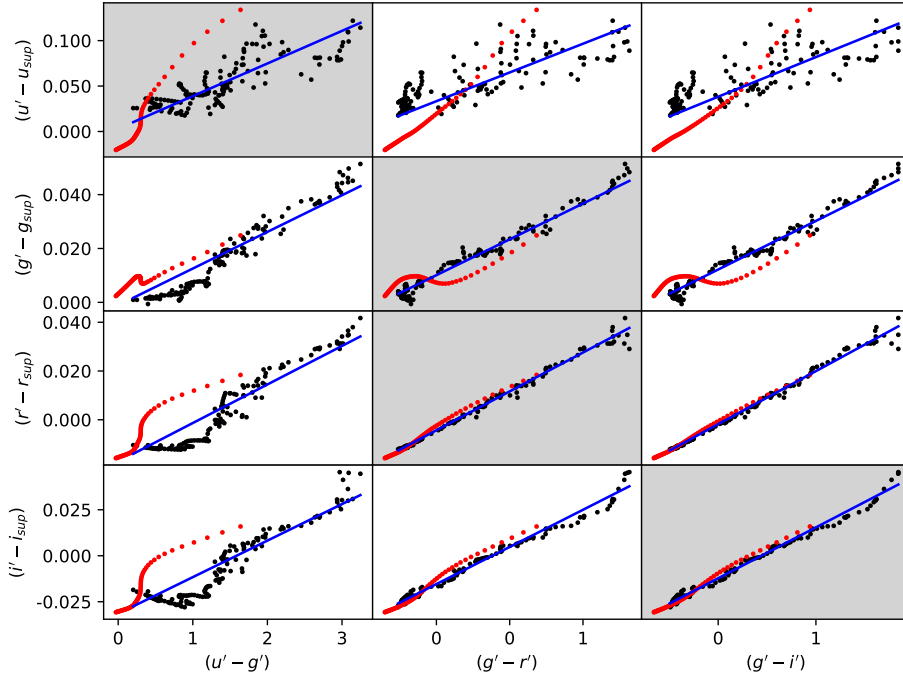| Correction | Diagnostic | y-intercept, $\phi$ | Colour Gradient |
|---|---|---|---|
| $(u' - u_s)$ | $(u' - g')$ | 0.003 | 0.036 |
| | $(g' - r')$ | 0.033 | 0.063 |
| | $(g' - i')$ | 0.038 | 0.044 |
| $(g' - g_s)$ | $(u' - g')$ | -0.001 | 0.014 |
| | $(g' - r')$ | 0.010 | 0.027 |
| | $(g' - i')$ | 0.012 | 0.018 |
| $(r' - r_s)$ | $(u' - g')$ | -0.017 | 0.016 |
| | $(g' - r')$ | -0.004 | 0.032 |
| | $(g' - i')$ | -0.002 | 0.022 |
| $(i' - i_s)$ | $(u' - g')$ | -0.031 | 0.020 |
| | $(g' - r')$ | -0.015 | 0.040 |
| | $(g' - i')$ | -0.012 | 0.028 |



Figure 2.2: The difference between the classic SDSS photometric system, and the ULTRACAM SuperSDSS filters on the NTT, as a function of SDSS colours, are calculated for model atmospheres. Red points are Koester white dwarf models, black points are Phoenix main sequence model atmospheres, and the blue line is the best fit straight line to both datasets. When applying colour corrections, the highlighted relations were used.

### 2.5.3 Calculating comparison star magnitudes

Equation 2.1 was used to calculate the zero points in each band from the standard star, for the SDSS photometric system. The comparison star SDSS magnitudes are then determined. As the colour term corrections are dependent on SDSS colours, an iterative approach was used to converge on these values. The SDSS magnitudes are related to the instrumental magnitudes by:

$$u' = u_{\mathrm{inst},0} + u_{\mathrm{zp}} + c_{\mathrm{u,sup}}(u' - g')$$
$$g' = g_{\mathrm{inst},0} + g_{\mathrm{zp}} + c_{\mathrm{g,sup}}(g' - r')$$
$$r' = r_{\mathrm{inst},0} + r_{\mathrm{zp}} + c_{\mathrm{r,sup}}(g' - r')$$

Initially, $u', g', r'$ magnitudes are set equal to the instrumental magnitudes, and a new set of $u', g', r'$ magnitudes are calculated. The new values are then used to repeat the calculation until a new iteration produces no change, typically after $\sim$4 loops. For the data taken with $u_{\mathrm{sup}}, g_{\mathrm{sup}}, i_{\mathrm{sup}}$ filters, the process is identical but replaces $r$ with $i$.

### 2.5.4 Producing a flux-calibrated target lightcurve

Finally, the target lightcurves can be calculated. We need to both correct the target star lightcurve for transparency variations, and convert from counts to calibrated fluxes. As we are producing a flux-calibrated lightcurve in the SDSS photometric system using a significantly different photometric system, the simple ADU ratio between the target and comparison is insufficient. Consider the target star $g'$ magnitude and flux, $g^t, F^t$, and comparison star $g'$ magnitude and flux, $g^c, F^c$:

$$g^t = g^t_{\mathrm{inst},0} + g_{\mathrm{zp}} + c_{\mathrm{g,sup}}(g' - r')^t$$
$$g^c = g^c_{\mathrm{inst},0} + g_{\mathrm{zp}} + c_{\mathrm{g,sup}}(g' - r')^c$$

since,

$$g^t - g^c = -2.5\log\left(\frac{F^t}{F^c}\right)$$

we can write

$$
\begin{aligned}
\frac{F^t}{F^c} &= 10^{-0.4(g^t_{\mathrm{inst},0} - g^c_{\mathrm{inst},0})} \cdot 10^{-0.4 c_{\mathrm{g,sup}} \left( (g'-r')^t - (g'-r')^c \right)} \\
\frac{F^t}{F^c} &= \frac{ADU^t}{ADU^c} \cdot K^{t,c}
\end{aligned}
$$

where $K^{t,c} = 10^{-0.4 c_{\mathrm{g,sup}} \left( (g'-r')^t - (g'-r')^c \right)}$. This accounts for differences in wavelength response between the two systems when calculating the flux ratio, and is applied to each frame. The $(g'-r')^t$ magnitudes are calculated using a sigma-clipped mean instrumental magnitudes computed from all frames in the observation. In practice, the factor $K^{t,c}$ varies from $\sim 1.0 - 1.1$ across the three systems.

ASASSN-16kr was observed in both the standard SDSS filters in 2018, and the super SDSS filters in 2019. This presented an opportunity to compare the corrected 2019 data with the fluxes observed in 2018. Additionally, both ASASSN-16kr and SSSJ0522-3505 use multiple standard stars across observations, which should agree if the calibration has been done correctly. In all cases, the flux-calibrated lightcurves were similar and the white dwarf colours consistent, suggesting that this method of flux calibration is indeed accurate.

To account for residual error in flux calibration, we add a 3% systematic error in quadrature to the white dwarf fluxes when fitting for the effective temperature.

## 2.6 Catalogue of observations

The observations analysed in this work span the full decade from 2011, through to 2021, and have been taken from multiple sites as the instruments move from telescope to telescope. To aid with the readability, a key is provided in Table 2.3 of the acronyms used for instruments and telescopes.

| Acronym | Expansion |
|---------|-----------|
| NTT | New Technology Telescope |
| GTC | Gran Telescopio Canarias |
| TNT | Thai National Telescope |
| WHT | William Herschel Telescope |
| VLT | Very Large Telescope |
| HCAM | HiPERCAM |
| UCAM | ULTRACAM |
| USPEC | ULTRASPEC |

Table 2.3: Acronyms used in the observation summaries.

# Chapter 3

# Modelling techniques and methodology

In the preamble, give the short version of "we can extract a lot of data from eclipsing CVs" etc. Also bring up that, because a CV is so compact, the population of eclipsers is actually fairly high. Talk about the state of stellar modelling, and say that we can apply it to CVs. Talk about how we can use this to convert eclipse modelling characterisation directly to an empirical mass loss rate, slash AML rate.

## 3.1   Eclipse modelling of a CV

Talk about how this is already a well-established method (Wood & Crawford, 1986; Savoury et al., 2011; McAllister et al., 2017, 2019), and its advantages over spectroscopic modelling and superhumping period excess.

Describe the model, i.e. its components and its parameters, and how it can be converted to physical parameters if we have the period and white dwarf temperature. Probably do two subsections for that. Point out that this is only possible due to *CAM - refer to Wild et al. (2021) for a pre-written version of this, and tweak it a bit. This will likely be quite a lengthy section, don't be afraid to break it up into subsections.

### 3.1.1   Capturing flickering with Gaussian Processes

Explain GPs from scratch, and get into detail about which kernels you're using.

## 3.2   The optimisation problem

Here I should discuss the problem of searching 15 dimensions for the best solution - then point out how much worse it is with 100+ dimensions. Here, I should put in some illustrative model fitting - perhaps a graph with steps vs. ln(like) for 1D, 5D, 10D, 15D? Dunno yet. Think about it. Alternatively, just make "MCMC Fitting" the section heading, and get straight into it. Mention binning eclipse lightcurves here as a primary mitigation strategy for the highly complex parameter space

### 3.2.1   Hierarchical model structure

This is going to take some work. Fit synthetic lightcurves with various amounts of noise, (5%, 10%, 20%?), and compare convergence times and posterior widths as

a function of noise. Do this with one eclipse, then with three eclipses of the same band, then with three eclipses in each of three bands. I should see an improvement in final probability distribution with more eclipses, since they can communicate.

Also, I need to come up with a way to demonstrate the potential to break degeneracies. Some lightcurves might be produced by two different parameter vectors, e.g. disc and donor might look similar to each other.

### 3.2.2 MCMC Fitting

I need to talk about the MCMC aspect of the fitting. Obviously explain MCMC fitting from scratch, but also make sure you explain the stretch move thing, ensemble sampling,

### 3.2.3 Parallel Tempering

Make sure you point out the downfall of PT - it's not suitable for more than 5 parameters! We seem to get away with it by using a lot of walkers, perhaps?

## 3.3 Evolutionary modelling

# Chapter 4

# The case of three strange white dwarfs

# Chapter 5

# Characterisation of 11 cataclysmic variables

# Bibliography

Allard F., Homeier D., Freytag B., 2012, in Richards M. T., Hubeny I., eds, IAU Symposium Vol. 282, From Interacting Binaries to Exoplanets: Essential Modeling Tools. pp 235–242, doi:10.1017/S1743921311027438

Argiroffi C., Caramazza M., Micela G., Sciortino S., Moraux E., Bouvier J., Flaccomio E., 2016, A&A, 589, A113

Cannizzo J. K., 1993, ApJ, 419, 318

Cerutti B., Dubus G., Henri G., 2007, in Bouvier J., Chalabaev A., Charbonnel C., eds, SF2A-2007: Proceedings of the Annual meeting of the French Society of Astronomy and Astrophysics. p. 158

Choi J., Dotter A., Conroy C., Cantiello M., Paxton B., Johnson B. D., 2016, The Astrophysical Journal, 823, 102

Davis P. J., Kolb U., Willems B., Gänsicke B. T., 2008, Monthly Notices of the Royal Astronomical Society, 389, 1563

De Marco O., Passy J.-C., Moe M., Herwig F., Mac Low M.-M., Paxton B., 2011, MNRAS, 411, 2277

Dhillon V. S., et al., 2016, in Ground-based and Airborne Instrumentation for Astronomy VI. p. 99080Y (arXiv:1606.09214), doi:10.1117/12.2229055

Dotter A., 2016, The Astrophysical Journal Supplement Series, 222, 8

Dubus G., Otulakowska-Hypka M., Lasota J.-P., 2018, A&A, 617, A26

Eggleton P. P., 1983, The Astrophysical Journal, 268, 368

Gallet F., Bouvier J., 2013, A&A, 556, A36

Gänsicke B., et al., 2009, MNRAS, 397, 2170

Garraffo C., Drake J. J., Cohen O., 2015, ApJ, 813, 40

Garraffo C., Drake J. J., Cohen O., 2016, ApJL, 833, L4

Garraffo C., et al., 2018a, ApJ, 862, 90

Garraffo C., Drake J. J., Alvarado-Gomez J. D., Moschou S. P., Cohen O., 2018b, ApJ, 868, 60

Gossage S., Dotter A., Garraffo C., Drake J. J., Douglas S., Conroy C., 2021, ApJ, 912, 65

Hameury J. M., 2002, in Gänsicke B. T., Beuermann K., Reinsch K., eds, Astronomical Society of the Pacific Conference Series Vol. 261, The Physics of Cataclysmic Variables and Related Objects. p. 377

Hellier C., 2001, Cataclysmic variable stars: how and why they vary. Springer

Hoffmann S. M., Vogt N., 2022, New Astronomy, 92, 101722

Ivanova N., et al., 2013, A&ARv, 21, 59

Ivanova N., Justham S., Ricker P., 2020, Common Envelope Evolution, doi:10.1088/2514-3433/abb6f0.

James D. J., Jardine M. M., Jeffries R. D., Randich S., Collier Cameron A., Ferreira M., 2000, Monthly Notices of the Royal Astronomical Society, 318, 1217

Jeffries R. D., Jackson R. J., Briggs K. R., Evans P. A., Pye J. P., 2011, MNRAS, 411, 2099

Kalomeni B., Nelson L., Rappaport S., Molnar M., Quintin J., Yakut K., 2016, The Astrophysical Journal, 833, 83

Kato T., et al., 2017, PASJ, 69, 75

Knigge C., 2006, Monthly Notices of the Royal Astronomical Society, 373, 484

Knigge C., 2011, arXiv e-prints, p. arXiv:1101.1538

Knigge C., Baraffe I., Patterson J., 2011, Astrophysical Journal, Supplement Series, 194, 28

Kochukhov O., 2021, A&ARv, 29, 1

Koester D., 2010, Mem. Soc. Astron. Italiana, 81, 921

Kolb U., 1993, A&A, 271, 149

Kolb U., 2002, in Gänsicke B., Beuermann K., Reinsch K., eds, Astronomical Society of the Pacific Conference Series Vol. 261, The Physics of Cataclysmic Variables and Related Objects. p. 180

Kolb U., de Kool M., 1993, A&A, 279, L5

Kolb U., King A., Ritter H., 1998, MNRAS, 298, L29

Littlefair S. P., Dhillon V. S., Marsh T. R., Gänsicke B. T., Southworth J., Baraffe I., Watson C. A., Copperwheat C., 2008, MNRAS, 388, 1582

Liu W.-M., Li X.-D., 2016, ApJ, 832, 80

Livio M., Pringle J. E., 1994, ApJ, 427, 956

Matt S. P., Brun A. S., Baraffe I., Bouvier J., Chabrier G., 2015, ApJL, 799, L23

McAllister M. J., et al., 2017, MNRAS, 464, 1353

McAllister M., et al., 2019, Monthly Notices of the Royal Astronomical Society, 486, 5535

Meibom S., Mathieu R. D., Stassun K. G., 2007, ApJL, 665, L155

Meliani M., de Araujo J., Aguiar O., 2000, A&A, 358, 417

Moraux E., et al., 2013, A&A, 560, A13

Osaki Y., 1996, PASP, 108, 39

Paczyński B., 1967, Acta Astronomica, 17, 287

Paczynski B., 1976, in Eggleton P., Mitton S., Whelan J., eds, Vol. 73, Structure and Evolution of Close Binary Systems. p. 75

Pala A. F., et al., 2020, MNRAS, 494, 3799

Pala A. F., et al., 2021, MNRAS,

Parsons S. G., et al., 2017, MNRAS, 470, 4473

Passy J.-C., 2013, PhD thesis, University of Victoria (Canada)

Passy J. C., et al., 2011, in Schmidtobreick L., Schreiber M. R., Tappert C., eds, Astronomical Society of the Pacific Conference Series Vol. 447, Evolution of Compact Binaries. p. 107

Patterson J., 1998, PASP, 110, 1132

Patterson J., 2001, PASP, 113, 736

Patterson J., et al., 2005, PASP, 117, 1204

Paxton B., et al., 2015, The Astrophysical Journal Supplement Series, 220, 15

Pevtsov A. A., Fisher G. H., Acton L. W., Longcope D. W., Johns-Krull C. M., Kankelborg C. C., Metcalf T. R., 2003, ApJ, 598, 1387

Politano M., 1996, ApJ, 465, 338

Politano M., Weiler K. P., 2007, ApJ, 665, 663

Qian S. B., Dai Z. B., He J. J., Yuan J. Z., Xiang F. Y., Zejda M., 2007, A&A, 466, 589

Rappaport S., Joss P. C., Webbink R. F., 1982, The Astrophysical Journal, 254, 616

Rappaport S., Verbunt F., Joss P., 1983, ApJ, 275, 713

Reiners A., Mohanty S., 2012, ApJ, 746, 43

Reiners A., Basri G., Browning M., 2009, ApJ, 692, 538

Rezzolla L., Uryū K. ō., Yoshida S., 2001, MNRAS, 327, 888

Ritter H., 1985, A&A, 145, 227

Ritter H., 2010a, Memorie della Societa Astronomica Italiana, 81, 849

Ritter H., 2010b, Mem. Soc. Astron. Italiana, 81, 849

Ritter H., 2012, Memorie della Societa Astronomica Italiana, 83, 505

Ritter H., Kolb U., 1998, A&A Suppl., 129, 83

Ritter, H. Kolb, U. 2003, A&A, 404, 301

Savoury C. D. J., et al., 2011, Monthly Notices of the Royal Astronomical Society, 415, 2025

Schaefer B. E., 2010, ApJS, 187, 275

Schönberg M., Chandrasekhar S., 1942, ApJ, 96, 161

Schreiber M. R., Zorotovic M., Wijnen T. P. G., 2016, Monthly Notices of the Royal Astronomical Society, 455, L16

Shafter A. W., Bautista V., 2021, Research Notes of the American Astronomical Society, 5, 207

Shakura N., Sunyaev R., 1973, Astronomy and Astrophysics, 24, 337

Simonsen M., et al., 2014, J. Am. Ass. of Variable Star Observers, 42, 177

Smith D. A., Dhillon V. S., 1998, Monthly Notices of the Royal Astronomical Society, 301, 767

Smith J. A., et al., 2002, The Astronomical Journal, 123, 2121

Solheim J. E., 2010, PASP, 122, 1133

Southworth J., Tappert C., Gänsicke B. T., Copperwheat C. M., 2015, A&A, 573, A61

Spada F., Lanzafame A. C., Lanza A. F., Messina S., Collier Cameron A., 2011, MNRAS, 416, 447

Sparks W. M., Sion E. M., 2021, ApJ, 914, 5

Spruit H. C., Ritter H., 1983, A&A, 124, 267

Taam R. E., Bodenheimer P., Ostriker J. P., 1978, ApJ, 222, 269

Tout C. A., 2011, Pramana, 77, 199

Townsley D. M., Gänsicke B. T., 2009, ApJ, 693, 1007

Tremblay P. E., Bergeron P., 2009, ApJ, 696, 1755

Verbunt F., Zwaan C., 1981, A&A, 100, L7

Warner B., 1995, Astrophysics and Space Science, 232, 89

Warner B., O'Donoghue D., 1988, MNRAS, 233, 705

Watson C. L., Henden A. A., Price A., 2006, Society for Astronomical Sciences Annual Symposium, 25, 47

Webbink R. F., 1984, ApJ, 277, 355

Wickramasinghe D., Li J., Wu K., 1996, PASA, 13, 81

Wijnen T., Zorotovic M., Schreiber M., 2015, A&A, 577, A143

Wild J. F., et al., 2021, MNRAS,

Wood J., Crawford C., 1986, MNRAS, 222, 645

Wood J. H., Irwin M. J., Pringle J. E., 1985, Monthly Notices of the Royal Astronomical Society

Wright N. J., Drake J. J., 2016, Nature, 535, 526

Wright N. J., Drake J. J., Mamajek E. E., Henry G. W., 2011, The Astrophysical Journal, 743, 48

Wu K., Wickramasinghe D. T., Warner B., 1995, PASA, 12, 60

Zorotovic M., Schreiber M., 2010, in Kalogera V., van der Sluys M., eds, American Institute of Physics Conference Series Vol. 1314, American Institute of Physics Conference Series. pp 19–21, doi:10.1063/1.3536366

Zorotovic M., Schreiber M., Gänsicke B., 2011, A&A, 536, A42

# Appendix A

# Appendix

## A.0.1 Ephemeris data

ASASSN-16kr has existing ephemeris data in the literature (Kato et al., 2017), whereas SSSJ0522-3505 and ASASSN-17jf were reported with tentative period estimates. These were used as starting points, and eclipse times from this work were used to refine the $T_0$ and $P$ for all three systems. Only ULTRACAM eclipse timings were used to calculate the ephemerides in this paper.

To calculate the time of white dwarf mid-eclipse for each observation, the numerical derivative of the flux was fit with a a double-Gaussian model, as described in Wood et al. (1985). Ideally, the derivative shows a negative peak at white dwarf ingress, and a symmetrical positive peak at egress, and each would be equidistant from the white dwarf mid-eclipse time, $T_{\mathrm{ecl}}$. By fitting the double-Gaussian model to a smoothed, numerical derivative of the lightcurve using a Markov Chain Monte Carlo (MCMC) method using a Gaussian process to evaluate the log-likelihood, we obtain $T_{\mathrm{ecl}}$ with uncertainties for each eclipse.

For each observed $T_{\mathrm{ecl}}$, its eclipse number $N$ (the number of eclipses since $T_0$) could unambiguously be determined from prior ephemeris data. An MCMC algorithm was used to fit a straight line model to the independent variable $N$ and dependent variable $T_{\mathrm{ecl}}$, with a gradient $P$ and intercept $T_0$. The model accounts for potential systematic differences in timing accuracy between instruments by also having variable error scale factors applied to all eclipses observed with a specific instrument, e.g. the timing reported for eclipses observed with ULTRACAM may be systematically offset from reality, and the errors associated with those observations might need to be larger than reported to be consistent with data from other instruments. The prior distribution assumed for these error factors

48

was log-uniform ranging from 0.01 to 100, which favours the smallest factor consistent with the data. The values of $N$ for each system were chosen to minimise the covariance between $T_0$ and $P$.
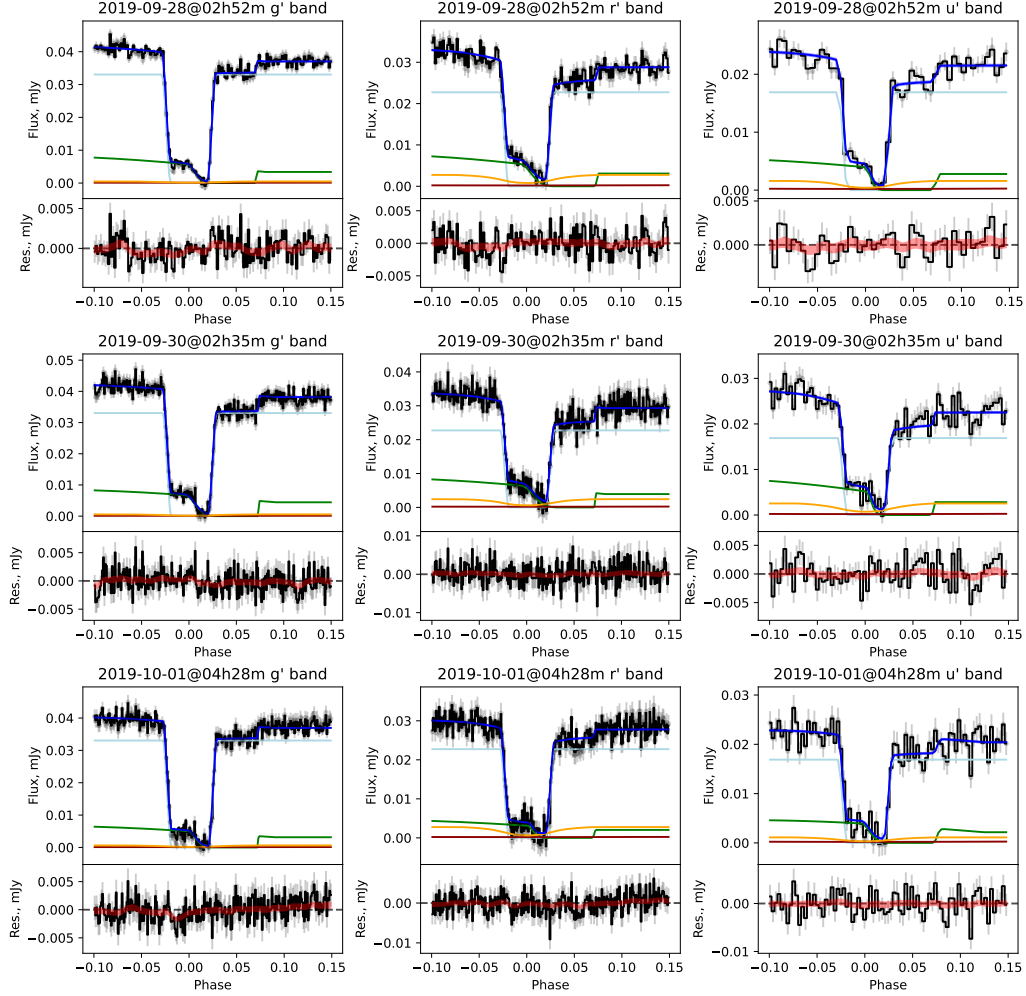
# A.1  Lightcurves

Figure A.1: ASASSN-17jf lightcurve models. *Top*: grey points are the observed flux; black line is the observed flux, with the mean Gaussian process sample subtracted; the dark blue line is the mean lightcurve model, and the blue band is the standard deviation on this in the MCMC chain. The components of the model are also shown: the light blue line is the white dwarf flux, green line is the bright spot, orange line is the disc, and the red line is the donor. *Bottom*: The residuals between the data and model are plotted as the black line, with grey error bars. The Gaussian process 1-sigma region is shown as a red band.
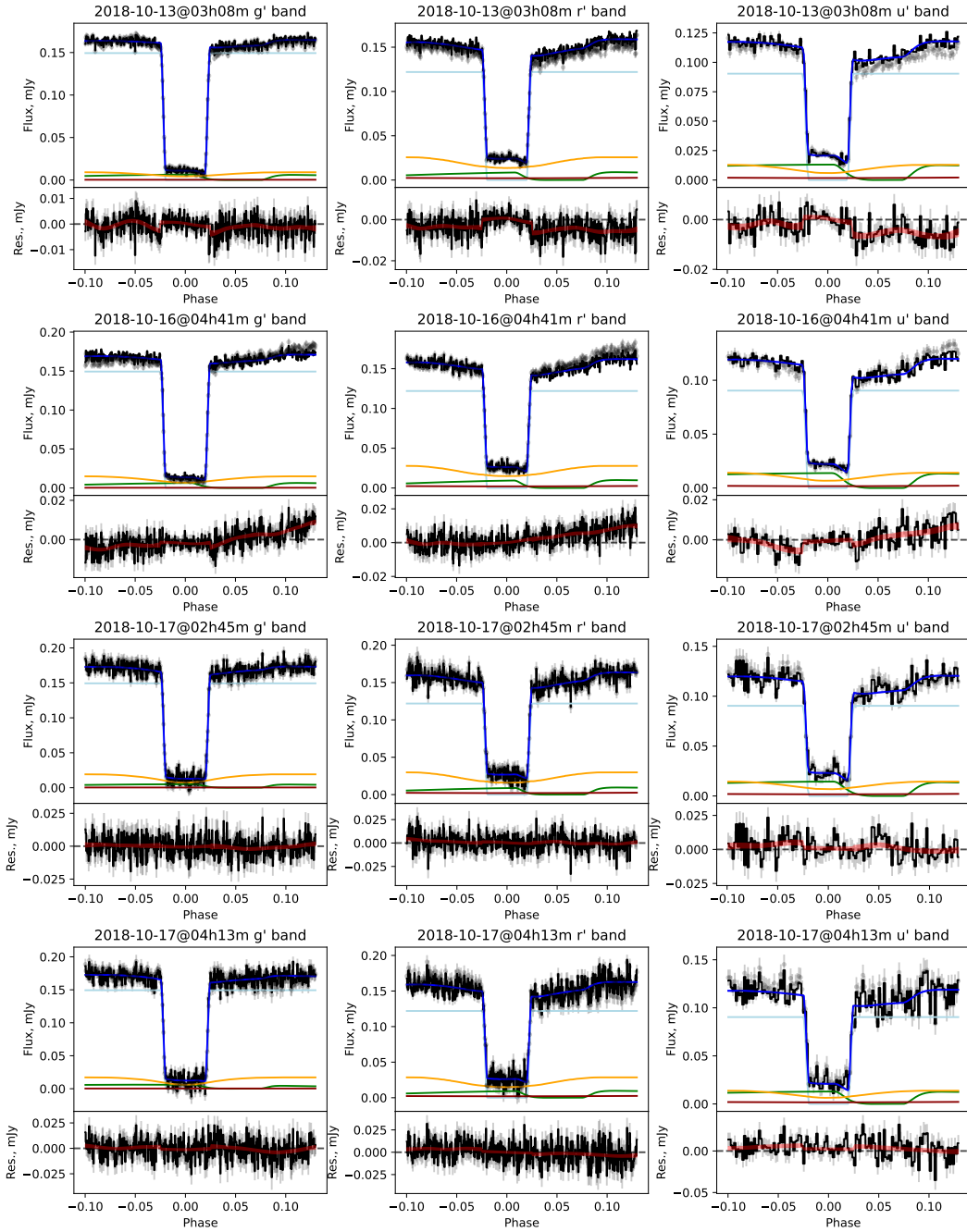
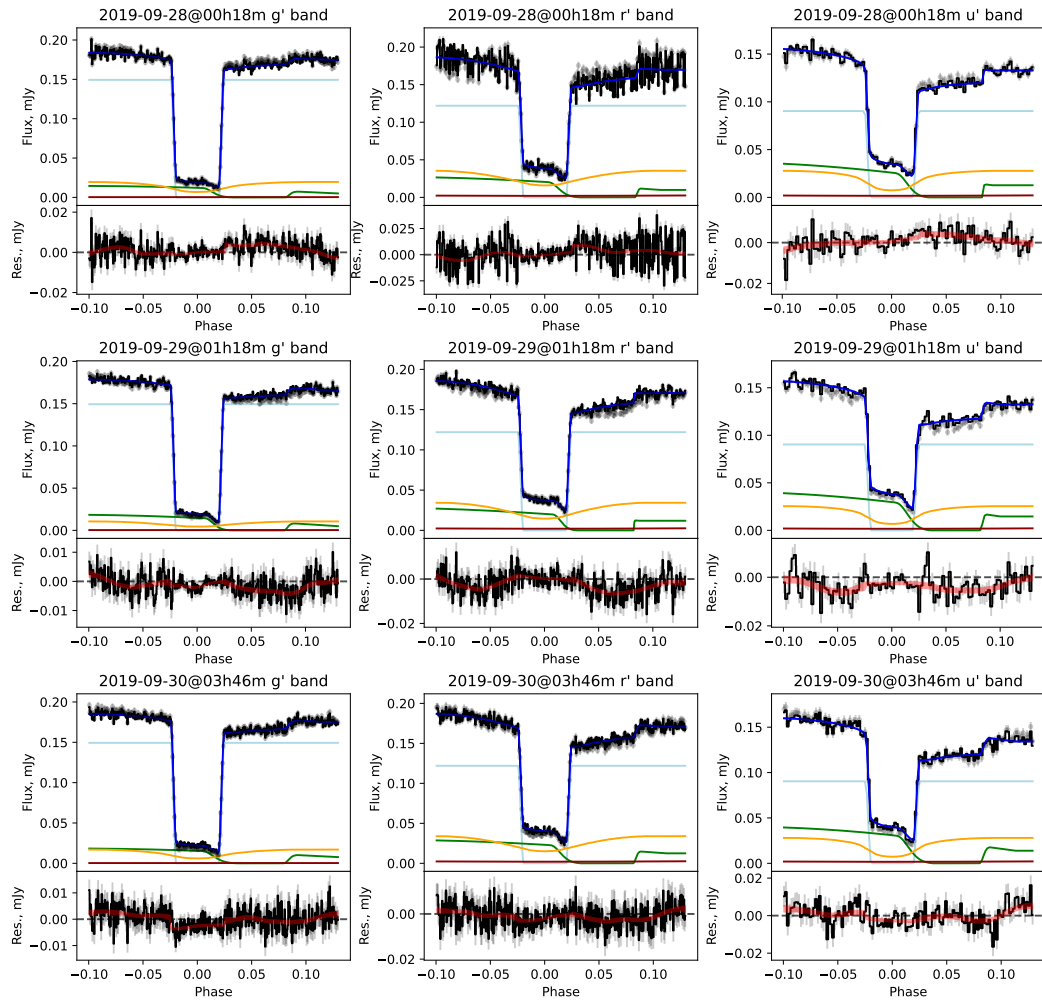Figure A.2: ASASSN-16kr lightcurve models. Symbols are the same as Figure A.1

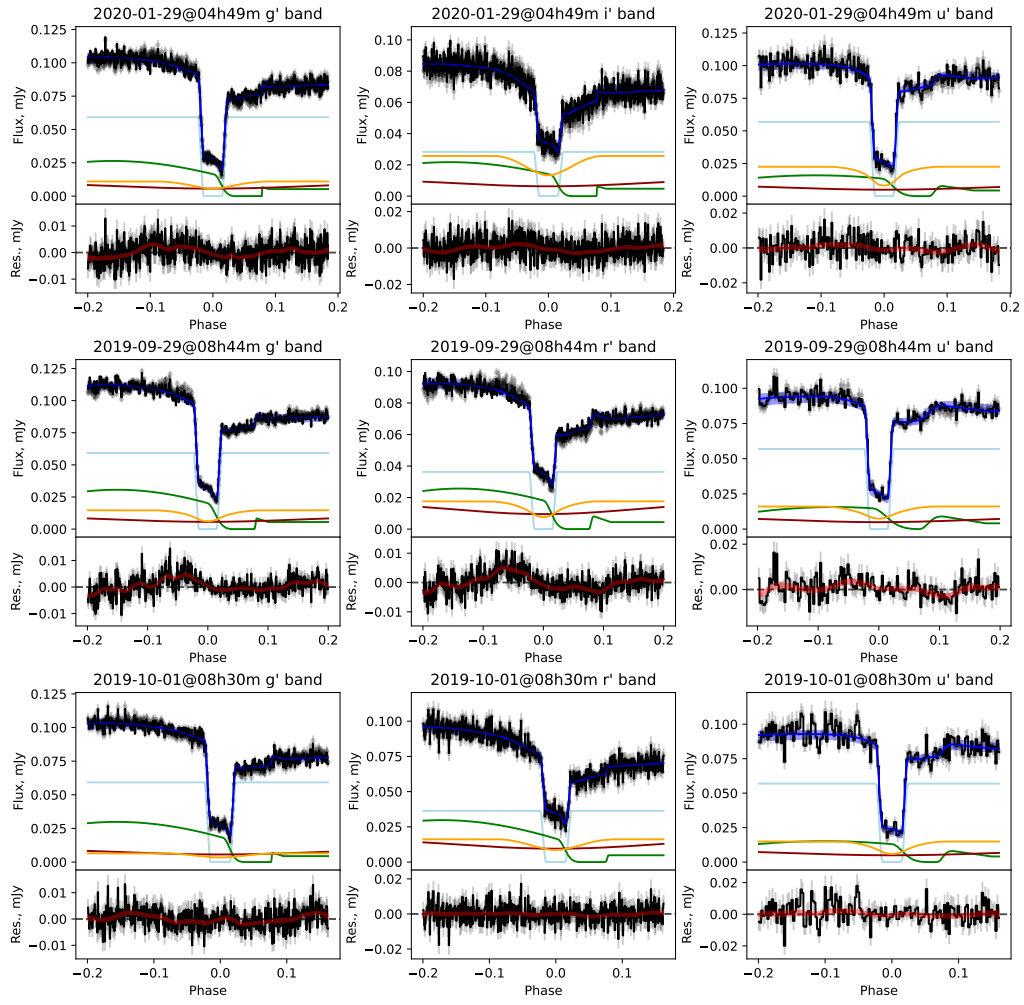Figure A.3: ASASSN-16kr lightcurve models (cont.)

Figure A.4: SSSJ0522-3505 lightcurve models. Symbols are the same as Figure A.1